Wear 520-521 (2023) 204654

Contents lists available at ScienceDirect

Wear

journal homepage: www.elsevier.com/locate/wear

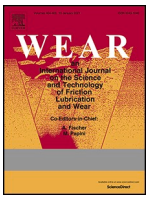

Effect of substrate bias voltage on structural and tribological properties of W-Ti-C-N thin films produced by combinational HiPIMS and DCMS co-sputtering

S.A. Ataie [a], M. Soltanieh [a,*], R. Naghizadeh [a], A. Cavaleiro [b,c], M. Evaristo [b], F. Fernandes [b], F. Ferreira [b,c]

[a] Iran University of Science and Technology, School of Metallurgy and Materials Engineering, Narmak, Tehran, 16846-13114, Iran
[b] University of Coimbra, CEMMPRE - Centre for Mechanical Engineering Materials and Processes, Department of Mechanical Engineering, Rua Luís Reis Santos, 3030-788, Coimbra, Portugal
[c] LED&Mat-IPN, Instituto Pedro Nunes, Laboratório de Ensaios Desgaste e Materiais, Rua Pedro Nunes, 3030-199, Coimbra, Portugal

ARTICLE INFO

Keywords:
PVD coatings
Surface topography
Indentation
Wear testing
Cutting tools

ABSTRACT

Protective multi-component thin films at the surface of cutting tools have been significantly developed to reduce wear and friction. The present work investigates the effect of substrate bias voltage on the structural-tribological relations of W-Ti-C-N thin films produced by HiPIMS and DCMS co-sputtering. Chemical analysis of the coatings is obtained and composite phase structure is revealed. Morphology of the coatings illustrates that defectless surfaces may be achieved. Topographical parameters are investigated by employing graphical software. Indentation, scratch and pin-on-disk tests (pin is AISI 52100 steel) are applied to study mechanical behaviors of the films. To produce a wear-resistant film, a median bias voltage (−60 V) and as a result, optimum content of tungsten concentration (19.2 at. %), grain size (42.8 nm) and average peak interval (188 nm) is required. Finally, a model based on the representative volume element is developed to show crack propagation and delamination.

1. Introduction

One of the first generations of hard protective coatings is TiN thin film system developed since 1980 [1–3]. To gain higher hardness and improved tribological performances, some elements were added to these films. Elements such as Cr, Mo, V, Nb and W (elements of the IVB, VB and VIB columns in the periodic table) were selected [4–7]. Also, Al and Si are other suitable candidates to do so [8,9]. Moreover, other researchers found out that adding carbon to TiN films can be a promising choice to use in mechanical parts [10,11]. Hence, multi-component coatings could be excellent candidates to satisfy severe mechanical conditions. As tungsten-based compounds [12] are one of the hardest materials in nature, some efforts have been made to produce tungsten nitride/carbide coatings [13–16]. Consequently, it is predictable that the W-Ti-C-N system could be one of the best choices to give a desirable tribological performance. This kind of film produced by conventional sputtering have been deposited since 2000 [17–22]. The mechanical and tribological properties of these films were examined by indentation, scratch and pin-on-disk testing. However, the exact information about the structural features (like surface topographical parameters) and mechanical properties (e.g. fracture/crack pattern) of this system have not been reported yet.

Multielement coatings which are composed of ceramic phases, have been extensively used in machining industries [9]. This is due to their higher thermal stability and hardness values rather than metallic coatings. However, the applications of these ceramic materials have their own limitations. Although the hardness of these materials is high enough, unlike metallic thin films [23], fracture toughness and adhesion to the substrate are the main issues which can deteriorate tribological properties [24–26]. These thin films which are submitted to severe conditions, should withstand high constant and variable loads. Therefore, under fixed and cyclic loads, these films must have the ability to prevent crack initiation and propagation which can delay delamination, peeling and brittle fracture [27–30]. Employing defectless and compact films with nano-sized grains and interlayers can guarantee wear-resistant coatings with desirable toughness and adhesion [31–33]. These materials with higher crack resistance [34] are the best candidates to coat metallic components. Moreover, like the model presented by

* Corresponding author.
E-mail address: mansour_soltanieh@iust.ac.ir (M. Soltanieh).

https://doi.org/10.1016/j.wear.2023.204654
Received 17 September 2022; Received in revised form 30 January 2023; Accepted 6 February 2023
Available online 10 February 2023

Fleming and Suh [35], hazardous microstructure (surface structure with subsurface voids and pores) production must be characterized to avoid catastrophic fracture during service conditions. Subsurface voids can join together simply and then quick delamination may occur.

The vapor deposition methods (physical or chemical) are promising processes to present high-quality thin films. In general, physical vapor deposition (PVD) processes are more efficient (e.g. energy consuming factor) in obtaining coatings with good mechanical and tribological properties [36–39]. To satisfy industrial conditions (e.g. higher deposition rate and lower temperature/energy consumption) and technological aspects (like higher surface uniformity without defects like macroparticles) simultaneously, magnetron sputtering is employed more than the other vacuum processes like arc and evaporation methods [40,41]. So far, direct current magnetron sputtering (DCMS) is the usual set-up employed for depositions. However, it has its limitations, like lower plasma ionization and low energetic particles received at the substrate surface [42]. Therefore, high power impulse magnetron sputtering (HIPIMS, also called iPVD, which means ionized type of PVD [43]) was developed to overcome these shortcomings. Recently, this method started to be preferred due to the higher particle mobility at the substrate surface and, as a result, higher coatings densities (without pores and open boundaries) are obtained. Generally, uniform nanostructured films are of great importance since these features influence the mechanical responses of materials [44]. In the sputtering deposition, there are process parameters affecting the structure quality of thin films such as substrate bias voltage [45,46], peak power density [47,48], reactive and plasma gas types and content [18,49,50], base pressure [51] and substrate temperature [18,52]. As mentioned before, because of higher particle energy in HIPIMS, rising substrate temperature is seldomly applied in HIPIMS [53]. Moreover, the use of different gas mixtures has been sufficiently studied [18,49,50], so substrate bias voltage and peak power density are challenging topics in HIPIMS depositions. Anyway, although some studies [44,54] investigate the mechanical properties of multielement thin films (more than three elements) produced by HIPIMS, tribological behavior of multielement coatings when substrate bias varies has been rarely researched [55].

In the present study, the effect of substrate bias voltage on the structural-mechanical properties of W-Ti-C-N thin films is analyzed. All in all, it is important to introduce optimum level of substrate bias voltage in HIPIMS processes to obtain excellent tribological properties. Hence, the main aim of this study is to investigate the structural-mechanical variations of W-Ti-C-N thin films prepared by combinational HiPIMS and DCMS. Substrate bias voltage value was changed from zero up to −80 V while other parameters were kept constant. Firstly, chemical bonds and phase characteristics of the coatings are studied. Then morphological and topographical features are analyzed. In addition, indentation (with low and high loads) and sliding tests (scratch and pin-on-disk tests) results are performed. Finally, a detailed discussion of adhesion and wear characteristics is presented. Furthermore, a model for a brittle fracture is proposed based on the representative volume element.

2. Materials and methods

2.1. Deposition conditions

W-Ti-C-N films were deposited with a HiPIMS power supply (HiPIMS Cyprium™ plasma generator, Zpulser Inc.) connected to a titanium (99.99%) square target and a continuous DC power source (Hüttinger PFG 7500 DC) connected to a tungsten carbide (99.95%) square target. For both targets, the dimensions were equal to 150 × 150 mm and 10 mm in thickness. In each deposition, silicon [100] 1.5 × 1.5 cm and steel (AISI D2) samples were used. The AISI D2 steel substrates (25 mm diameter and 8 mm thick) were tempered at 200 °C (60 HRC) and mirror polished using diamond paste (Ra ≈0.1 μm). Both, the steel and silicon substrates were cleaned in acetone and ethanol ultrasonic baths for 15 min each and glued with electric and thermal conductive glue (99.9% purity) onto an aluminum substrate holder that revolved at 23.5 rev/min around the central axis of the deposition chamber during the depositions. The substrate-to-target distance was kept at 80 mm. A base pressure lower than 3×10^{-4} Pa was achieved before the depositions using a system constituted by a rotary and a turbomolecular pump. Prior to all depositions, the substrate surface was etched using a pulsed DC power source (voltage = 340 V and current = 0.12 A) for 60 min. In order to enhance the W-Ti-C-N films adhesion to the substrates, a Ti layer was first deposited on the substrates surface and followed by a TiN layer. The first layer composed of Ti (10 min of deposition time in pure Ar plasma by HiPIMS at 0.4 Pa) and TiN (6 min of deposition time with 50% N_2 in the discharge gas at 0.8 Pa) was deposited prior to the main runs.

In this work, the target peak power (Pp) is defined as the product of peak voltage (Vp) × peak current (Ip). For all depositions, the peak power is nearly constant (60.7 KW). For both DCMS and HiPIMS, the average power (Pa) of deposition was kept constant at 700 W in all depositions. In HiPIMS, both the voltage and current waveforms consist of packets of oscillations with a duration (D) of 1800 μs. Each oscillation consists of a gradual increase of both the voltage and the current up to a maximum value during the on-time (t_{on} = 6 μs), followed by a gradual decrease down to zero before the beginning of the next oscillation. The oscillations period (T) was kept constant at 70 μs. More details about the oscillating current and voltage waveforms in DOMS can be found in reference [56]. To study the microstructure features and mechanical properties relationships, it was decided to change the substrate bias voltage with the values listed in Table 1.

2.2. Characterization methods

2.2.1. Micro-structure tests

The microstructure of the films was studied by scanning electron microscopy (SEM) using a Quanta 400FEG ESEM. All SEM micrographs were acquired with a 5 keV beam. To get SEM images, secondary electron detectors were applied. The composition of the films was evaluated by Energy Dispersive Spectroscopy (EDS). ZAF (atomic number-Z-, absorbance-A-, and fluorescence-F-) corrections were employed for EDS measurements. Also, for each sample, the element concentrations were evaluated after averaging the data from five different sites. Surface roughness was measured by AFM (Bruker Innova) in contact mode using a SiN tip with a radius lower than 10 nm.

The phase structure of the coatings was characterized by grazing incidence X-ray diffraction (GI-XRD) (Analytical X'Pert PRO MPD) with Cu Kα radiation (45 kV and 40 mA-λ = 1.54 Å) using a parallel beam in symmetrical θ–2θ geometry. Applied grazing angle was 1°.

The structural investigation of the deposited films was performed by employing UV Raman spectroscopy using a Renishaw inVia Raman microscope equipped with a He-Cd laser of 325 nm.

2.2.2. Mechanical tests

To measure mechanical properties of thin films, indentation techniques were used [57–59]. The hardness and Young Modulus of the films were measured by nano-indentation (Micromaterials Nano Tester) using a Berkovich diamond indenter. The values were obtained from the load–penetration depth curves, using a method developed by Oliver and Pharr [58]. Sixteen hardness measurements were performed for each

Table 1
Samples and parameters.

Sample code	Bias value [V]	Pp [KW]	Ip [A]	Vp [V]
S0	0	61	55	1105
S40	−40	59	54	1100
S60	−60	62	54	1140
S80	−80	61	53	1150

specimen. A 5 mN load was used in order to ensure an indentation depth lower than 10% of the coating thickness. Also, to investigate the fracture toughness of the coatings, different high load indents (100 mN, 450 mN-this level is the maximum value of nano-indentation tester- and 1N-with Vickers indenter-) in various sites of thin films were done.

The scratch test was used to evaluate the adhesion of the films. It was performed using a scratch tester, CSEM – REVETEST, with a Rockwell "C" diamond-tipped indenter with a spherical tip radius of 200 μm. A normal load was linearly increasing from 0 to 60 N, and the scratch speed was 10 mm/min and a loading rate of 100 N/min. Before testing, all samples and the indenter were cleaned with ethanol. An optical microscope was used to quantify the adhesive properties of the film.

The tribological behavior of the W-Ti-C-N films was evaluated by pin-on-disk tests in an ambient atmosphere (room temperature, 40% relative humidity and without lubrication) using 10 mm AISI 52100 balls as counterparts. Prior to the sliding wear tests, steel pins were sonicated in acetone. Then they were washed by distilled water and dried in hot air to remove surface contamination. All tests (three tests in each sample) were carried out with a linear speed of 0.1 m/s and a 5 N load during 2000 cycles. Also, to study wear rate trends, 500 and 4000 cycles tests were done. Cross-section profiles of the wear tracks were acquired using a 2D profilometer (MituToyo Surf test SV-500). The wear rate was determined from the average area of the wear track profiles taken from at least three profiles obtained at different locations. The wear tracks morphology was observed by scanning electron microscopy (SEM) using a Quanta 400FEG ESEM.

2.2.3. Softwares and modeling

In order to study fractal parameters, Gwyddion software (v. 2.60) was used. In addition, to calculate wear area of 2D profiles, Autodesk AutoCAD (v. 2022) software was applied. Moreover, to draw thin film structure and delamination procedure, Adobe Photoshop (v. 2021) and AutoCAD were employed. As can be seen from SEM images (Figs. 3 and 4), coatings are uniform and the average properties of one selected local area could be an indicator of the whole micro-structure. Hence, the structure model used as representative volume element (RVE) [60] could represent the continuum properties of the coating mass.

3. Results

3.1. Microstructure of the coatings

3.1.1. Chemical analysis

Table 2 presents the elemental composition of W-Ti-C-N thin films obtained from EDS analysis. As can be seen, by increasing bias potential, both metallic percentages (W + Ti) and nitrogen content in the coatings gradually increase. In contrast, carbon content gets lower values and oxygen (usual impurity in PVD processes [18,33]) is presented in low amounts (below 3.5 at%) and its content is influenced by the bias voltage. Hence, metals to nonmetals ratio increases when bias voltage increases (see the right column in Table 2). It must be mentioned that other impurities (like Ar, that can be incorporated in thin films with extremely low amounts [8]) contents are lower than 0.2 at. %. This trend can be explained by the energy and mass of particles reaching the substrate [42,46]. At higher levels of bias voltage, particles with higher mass weights (W and Ti ions/atoms) diffused and deposited to the coating more efficiently and nitrogen could be substituted for the carbon in the growing layer. On the one hand, nitrogen amounts in thin films are higher than carbon and on the other hand, nitrogen content rises while carbon content becomes less. As a result, the content of nitride compounds can grow gradually while the amounts of carbide compounds reduced significantly.

Table 2
Elemental percentage of thin films based on EDS analysis.

Sample code	W [at. %]	Ti [at. %]	N [at. %]	C [at. %]	O [at. %]	M/NM [%]
S0	17.4	13.7	44.8	20.4	3.5	45.26
S40	18.6	13.7	45.8	20.0	1.9	47.71
S60	19.2	13.9	46.1	18.0	2.7	49.55
S80	17.0	16.8	47.9	15.9	2.2	51.21

Fig. 1 shows the grazing incidence X-ray diffractograms of the coatings. Because of low peak intensities, it can be concluded that hybrid/composite phase structure (crystalline phases and amorphous phase) are obtained. To add to it, the amorphous phase is the major phase in all thin films while some low content nano-crystalline phases (according to the Scherer equation, maximum crystallite size is 16 nm) can be seen. High content of the amorphous phase in the thin films produced by co-sputtering in the presence of high nitrogen ratio ($P_{N2}/P_{Ar} = 0.5$) is usual [4,15]. Moreover, crystalline phases can be attributed to WN (Ref. Code = 96-153-8665), W_2N (Ref. Code = 00-025-1257), WC (Ref. Code = 01-073-0471), WC_{1-x} (Ref. Code = 00-020-1316), TiN (Ref. Code = 00-038-1420), TiC (Ref. Code = 96-591-0092), $TiC_{0.2}N_{0.8}$ (Ref. Code = 01-076-2484). Peak broadening can be assigned to overlapping the XRD patterns of the abovementioned phases and nano-crystalline structure. Therefore, detecting the phase structure of W-Ti-C-N coatings by XRD patterns alone is nonsense and it requires more investigation.

Fig. 2 shows the Raman spectra of W-Ti-C-N thin films, illustrating narrow and wide peaks at low and high vibrational frequencies which are related to the acoustical and optical phonons [10]. It is worth mentioning that exact peak locations are not constant for all samples (or the other related works) because the phase and bond stoichiometries can present some variations [61]. Therefore, introducing peak location by wavenumber range is more logical. In these spectra, vibrational interactions of 145–157 cm^{-1} are attributed to the W_2N bonds (like the presentation in Ref. [15]). Peaks located at 480- 487 cm^{-1} are related to the WC bonds. Similar work [13] confirms this result. Low intensity peaks at 790-810 cm^{-1} can be attributed to the TiCN bonds. This result is in good agreement with the previous study [10]. Furthermore, peaks at 1350–1378 and 1550-1565 cm^{-1} are attributed to the D and G peaks of amorphous carbon (like reference [62]). Interactions at 2348-2351 cm^{-1} can be related to the CN bonds. This result and the findings presented by Chowdhury et al. [63] are alike. For carbide compounds, I_D/I_G can be a suitable indicator to show crystallinity. Moreover, the full width at half maximum (FWHM) of a sharp peak can be used as a crystallinity criterion [41]. As the FWHM of the right peak (2350 cm^{-1}) is similar for all the coatings, the left peak (150 cm^{-1}) was selected. FWHM of sample S60 is minimum (72 cm^{-1}). Nevertheless, a criterion based on peak intensities (including carbide and nitride phases simultaneously) could be more reliable (given in discussion section 4.1). All things considered (the data from Table 2, Figs. 1 and 2), it can be concluded that the WC, W_2N and $TiC_{0.2}N_{0.8}$ nano-crystalline phases are present in all coatings, whereas the amorphous carbon phase can be present since D peak in the Raman spectra is present for all films. The formation of WC and $TiC_{0.2}N_{0.8}$ phases was also observed in our previous work done by conventional sputtering [18]. To add to it, the existence of nano-crystalline tungsten nitride in the films means that the target can be sputtered with the decomposition of WC particles by higher plasma density (HIPIMS), and then nitrogen reacts with the species. However, because of lower intensities in Raman spectra and decreasing the C percentage in EDS analysis, amorphous carbon content is lower in samples S60 and S80 rather than in S0 and S40.

3.1.2. Morphology

Fig. 3a–d shows cross-sectional SEM images of W-Ti-C-N thin films. According to these images, it is clear that all the sample structures are compact and without any macro-defects (like pores and macro-particles [32]) which can be generated during sputtering. The thickness of the first layer (Ti + TiN) as well as the total thickness of the coatings are presented in all figures. The thickness of the first layer is slightly above

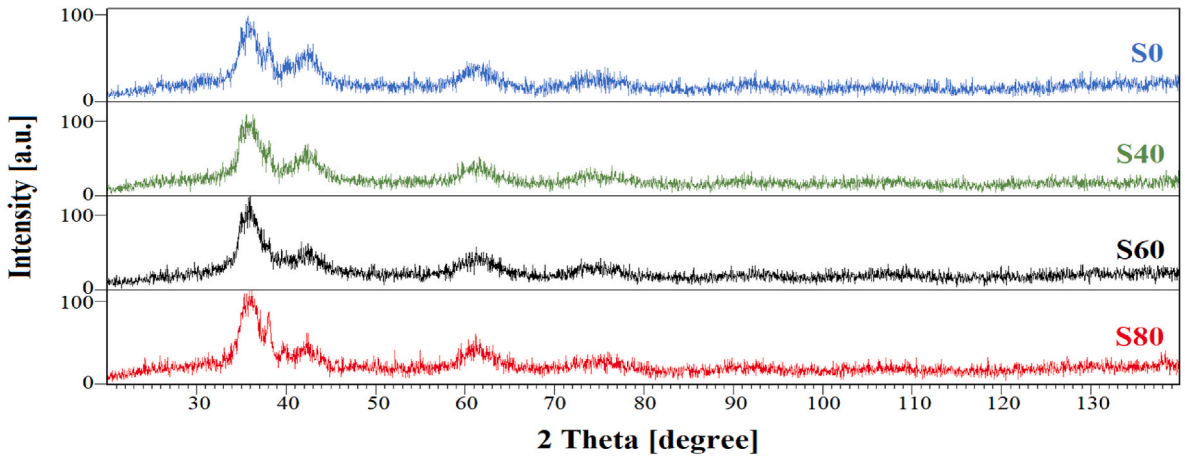

Fig. 1. GI-XRD diffractograms of thin films.

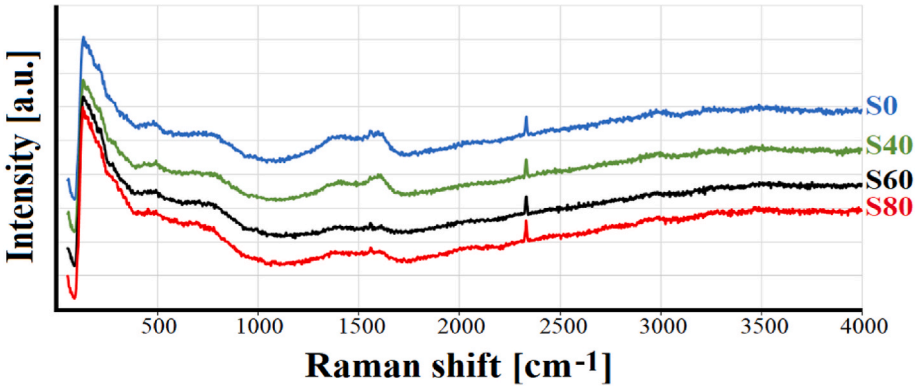

Fig. 2. Raman spectra of thin films.

100 nm, which guarantees favorable adhesion between the coating and substrate. It is obvious that deposition rates of samples S40 and S60 are more than samples S0 and S80. By fixing all the parameters and just increasing substrate bias voltage, the thickness is increased from 953 nm (S0) to 1070 nm (S40) and 1060 nm (S60) then decreased to 936 nm (S80). Moreover, it is important to mention that samples S0 and S40 illustrate fine columnar morphology while sample S60 has featureless morphology. Clear oblique columnar morphology can be observed in Fig. 3d for sample S80. However, at the first layer and second layer interface of samples S40 and S60 minor columnar growth is generated. Unlike metallic thin films [45,46], increasing bias voltage firstly enhances the deposition rate and then gets a considerable reduction. This trend could be explained by the energy distribution of particles received at the surface of the substrate/last deposited layer and the addition of reactive gas (nitrogen) [44]. Firstly, without any bias potential (sample S0), adatoms/ions are received and deposited on the surface in normal mode. By increasing bias voltage level, the energies of particles increase and growth rate gets the maximum value (samples S40 and S60). In this study, higher bias voltages (sample S80) can facilitate directional growth and result in columnar morphology. In contrast, a previous study [54] demonstrated that with increasing substrate bias voltage dense and featureless morphology takes place. The dissimilarity between the present work and the mentioned one [54] may be related to the sputtering parameters like temperature and pulse characteristics [56].

Fig. 4a–d shows the SEM images of W-Ti-C-N thin films (surface morphology of the coatings). All coatings, with the exception of S60 (Fig. 4c), show unequal and large grains. The S60 film presents uniform and ultra-small grains. The homogenous morphology of sample S60 can be a result of compact positioning (dense structure illustrated in Fig. 3c) of deposited particles. This similar outcome was mentioned elsewhere [55]. Furthermore, all the grains in sample S60 (see yellow grains in Fig. 4c) are quite small (below 100 nm) while there are macro-grains in other samples. These macro-grains (more than 100 nm) are identified by red arrows and boundaries in Fig. 4a, b and 4d. Grains in sample S0 (Fig. 4a) do not have a specific shape while they are nearly circular in sample S40 (Fig. 4b) and textured in sample S80 (Fig. 4d). This textured oblique shape of grains in sample S80 is the result of oblique columnar growth which is characterized by red boundaries in Fig. 3d. As the surface roughnesses of all samples are extremely low (lower than 1.59 nm, see Table 3), their image contrast and grains are not highly qualified. Therefore, AFM set-up could be useful to investigate surface features of W-Ti-C-N thin films.

To study the coatings topography, 3D-AFM images of W-Ti-C-N thin films are shown in Fig. 5a–d. It is clear that the sample S60, with peaks at the maximum of 20 nm and valleys at a minimum of −15 nm in Fig. 5c, has the lower roughness amplitude in comparison to the other films see Fig. 5a, b and 5d. It is obvious at a glance that because of the identical process to deposit samples (utilizing HIPIMS and clean room chamber), the height distribution and roughness values of the films are nearly equivalent. According to Table 3, roughness and fractal dimension are almost equal for all the coatings ($1.18\ nm \leq Ra \leq 1.31\ nm$, $1.49\ nm \leq Rq \leq 1.59\ nm$ and $2.40 \leq D \leq 2.43$). The minimum roughness data of sample S60 could be significant for mechanical properties. Nevertheless, the traditional explanations of surface geometry are based on average and root mean square roughnesses (Ra and Rq), however, they cannot describe the total features of surface topography [64]. Therefore, for a detailed description of surface geometry, graphical analysis was employed. To get the fractal parameters listed in Table 3, segmentation

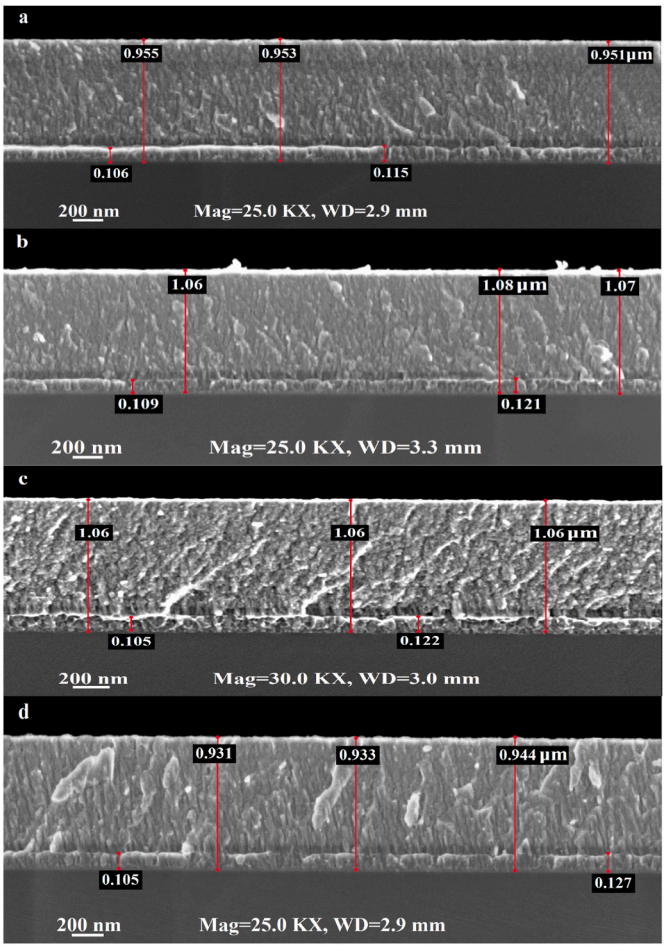

Fig. 3. Cross-sectional SEM images of thin films; (a) S0, (b) S40, (c) S60, (d) S80.

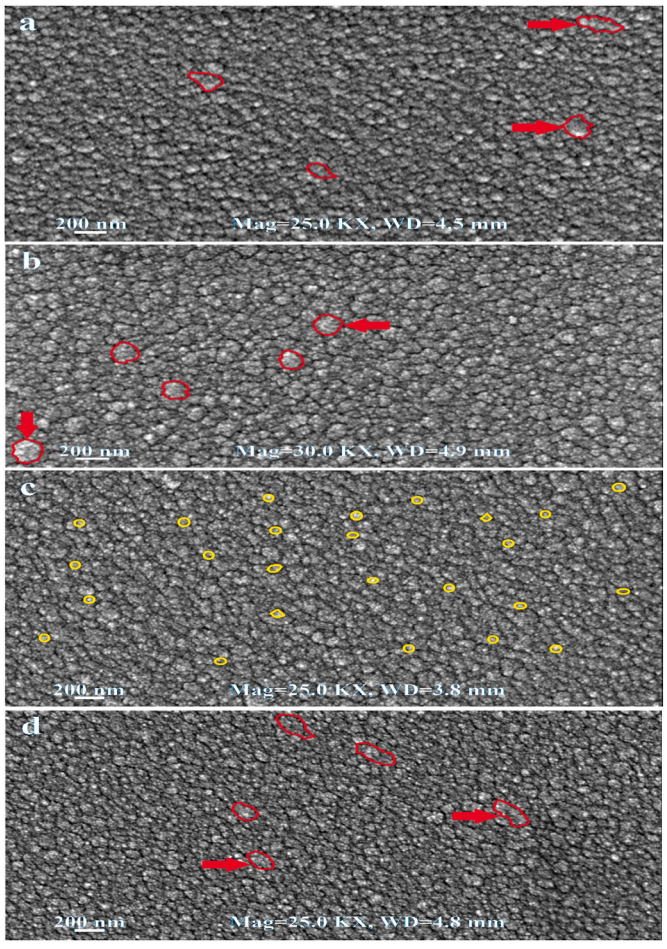

Fig. 4. Top-view SEM images of thin films; (a) S0 with vague grain shape, (b) S40 with circular grain shape, (c) S60 with fine grains, (d) S80 with textured grains .

method and texture profiles are applied (see Figs. M1 and M2 in the supplementary file). By increasing substrate voltage, average peak interval (API) increases up to 188 nm and then decreases. For grain size (d) in Table 3, this trend is reversed. Other parameters (grain density-GD-, skewness-Sk- and kurtosis-Ku-) follow no obvious trend. For sample S60, grain density (302.2 μm^{-2}) and kurtosis (2.83) are maximum. Among all the coatings, only S80 gets negative values of skewness. As a consequence, some extended grains are presented with red boundaries in Fig. M1d in the supplementary file. This result is in good agreement with the SEM image of S80 (Fig. 4d).

3.2. Mechanical properties of the coatings

3.2.1. Indentation characteristics

Fig. 6 presents the hardness and toughness parameters (H/E and H^3/E^2) of W-Ti-C-N coatings, based on load-indentation depth graphs with a maximum load of 5 mN (see Fig. M3 in the supplementary material). Strong and clear pop-in cannot be observed in load-displacement graphs. Like the discussion given in Ref. [37], this result is probably due to the low dislocation densities at these low values of indent loads. Increasing substrate bias voltage, firstly increases hardness and toughness values up to maximum values (sample S60), but with further increase in bias potential these mechanical properties decrease significantly (sample S80). Hence, it is clear that sample S60 gets the higher values of hardness (29.2 GPa), H/E (0.116) and H^3/E^2 (0.4). It must be noted that sample S40 gets the high hardness of 19.7 GPa but the toughness parameters (H/E and H^3/E^2) are not high enough to withstand severe conditions. However, these high values of hardness and toughness could be a sign of high stiffness values related to the ceramic phases (WC-W_2N-$TiC_{0.2}N_{0.8}$) plus composite structure. This result is in good agreement with the previous works [11,22]. Moreover, fracture toughness can be measured by high-intensity indentation forces (crack resistance evaluation) [26]. Therefore, to investigate this feature, 100 mN, 450 mN and 1 N forces were applied to the coatings. Fig. 7a–d shows the SEM images of the crack and spallation shapes of W-Ti-C-N thin films with 450 mN indentations. Similarly, Fig. 7á-7d´ show the SEM images of the crack and spallation shapes of W-Ti-C-N coatings with 1 N indentations load. Since there are no cracks with 100 mN indentations in the coatings, the SEM images are not presented here (see Fig. M4 in the supplementary file). Furthermore, with 450 mN loading, S0, S40 and S80 samples circumferential cracks can be observed and, delamination and chipping occur which are an indicator of brittle coatings [30]. It is important to mention that the classical equation used for calculating fracture toughness ($Kc = \alpha \times E^{0.5} \times H^{-0.5} \times P \times c^{-1.5}$ [65]) cannot be employed here, because the coating thickness is not enough to bear these high loads (more than 250 mN) without substrate influence [57,59]. As can be seen from Fig. 7, sample S60 (unlike the other samples) gets no chipping or continuous crack path. By crack bridging (shown by red arrows), crack deflection (shown by blue arrows) and crack branching (shown by green arrows) sample S60 resistance to the crack growth is desirable. These toughening mechanisms (cracks bridging, deflecting and branching [24,25]) are not observed in the other coatings, so long continuous cracks can cause fracture and complete failure. Moreover, sample S80 shows a complete fracture which is detrimental to use in the machining industry.

Table 3
Fractal parameters of thin films based on AFM images.

Sample code	Ra [nm]	Rq [nm]	API [nm]	d [nm]	GD [μm^{-2}]	Sk [−]	Ku [−]	D [−]
S0	1.26	1.51	162	44.6	285.9	0.022	2.42	2.42
S40	1.31	1.59	174	44.3	254.3	0.035	2.31	2.40
S60	1.18	1.49	188	42.8	302.2	0.005	2.83	2.41
S80	1.27	1.53	161	45.7	285.4	−0.073	2.37	2.43

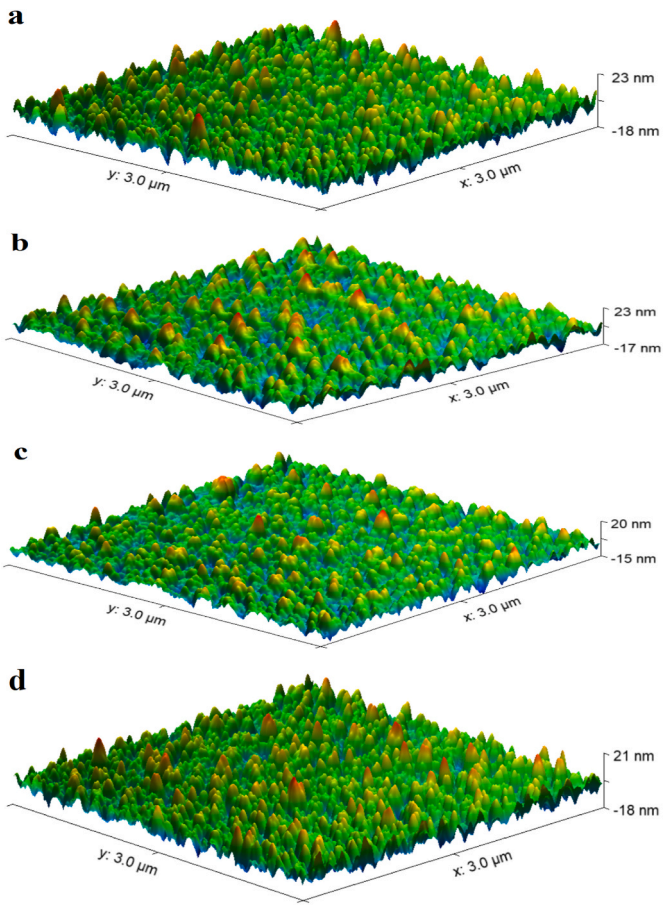

Fig. 5. AFM images of thin films; (a) S0, (b) S40, (c) S60, (d) S80.

3.2.2. Tribological characteristics

Excellent adhesion must be obtained at the coating-substrate interface to avoid massive delamination, when the coatings are submitted to mechanical stresses. Fig. 8 presents optical images of samples S0, S40, S60 and S80 of the scratches performed on the steel coated samples. According to the literature [27], there are three different critical loads to define adhesion between coating and substrate. L_C1 (known as cohesive failure limit) is given for the first cracking signs in the wear scar when L_C2 (known as adhesive failure limit) is an indicator for the initiation delamination of the coating and L_C3 belongs to the total coating delamination. Localized/partial delamination can be seen in all thin films while complete failure just occurred in sample S80 (L_C3, which is illustrated by a white arrow). These explanations are presented graphically in Fig. 8d. L_C1 is indicated by a red arrow and L_C2 is demonstrated by a blue arrow. Table 4 presents the average data of these critical loads for the thin films (three scratch lines were investigated; see Fig M5 in the supplementary material). In addition, according to Zhang et al. [28], to study the crack resistance of coatings it is useful to apply the equation of CPR = L_C1 (L_C2-L_C1). Crack propagation resistance (CPR) is defined to see the coating power to bear the loads after cracking (L_C1) without delamination (L_C2). As can be seen from Table 4, CPR of S60 is maximum while CPR is minimum in the case of S80. As a matter of fact, because of low cohesion and adhesion, large flakes (shown by yellow circles in Fig. 8d) and peeling can be observed in/out of the scratch line of sample S80. It is clear that because of catastrophic fracture and delamination, coating adhesion in sample S80 is not desirable and not suggested to use in industry.

Fig. 9 shows the friction coefficient evolution of WC-TiN thin films during a 2000 cycles pin-on-disk test. The related SEM images and 2D wear profiles are presented in Figs. 10 and 11, respectively. Because of high content of oxygen inside wear tracks (Fig. 10 á-d´), oxidative wear [16] can be the main wear mechanism during sliding. It is clear that sample S60, with an average friction coefficient of 0.49, has the lowest friction values that can contribute to a good performance in many tribological applications. A similar conclusion was presented in Ref. [55]. Friction coefficients of the other samples show higher values and their evolution during the tests presents significant fluctuations.

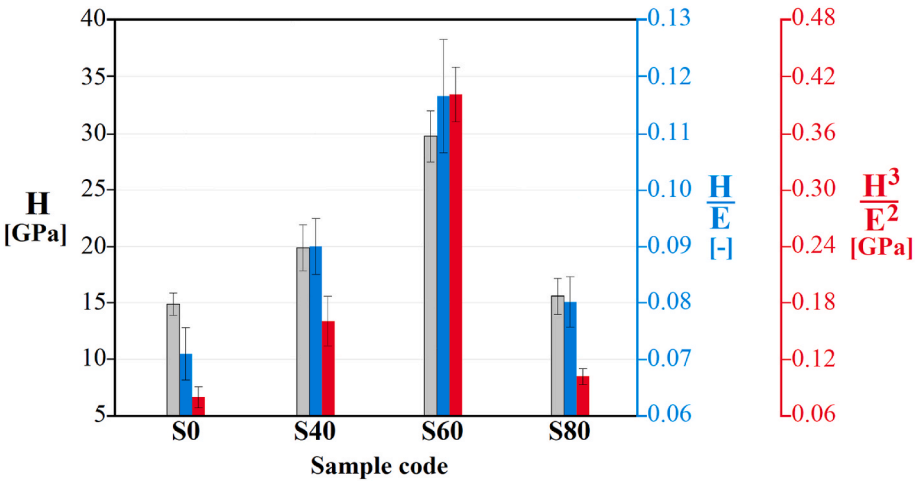

Fig. 6. Hardness and toughness parameters (H/E and H^3/E^2) of thin films based on low-force indentation.

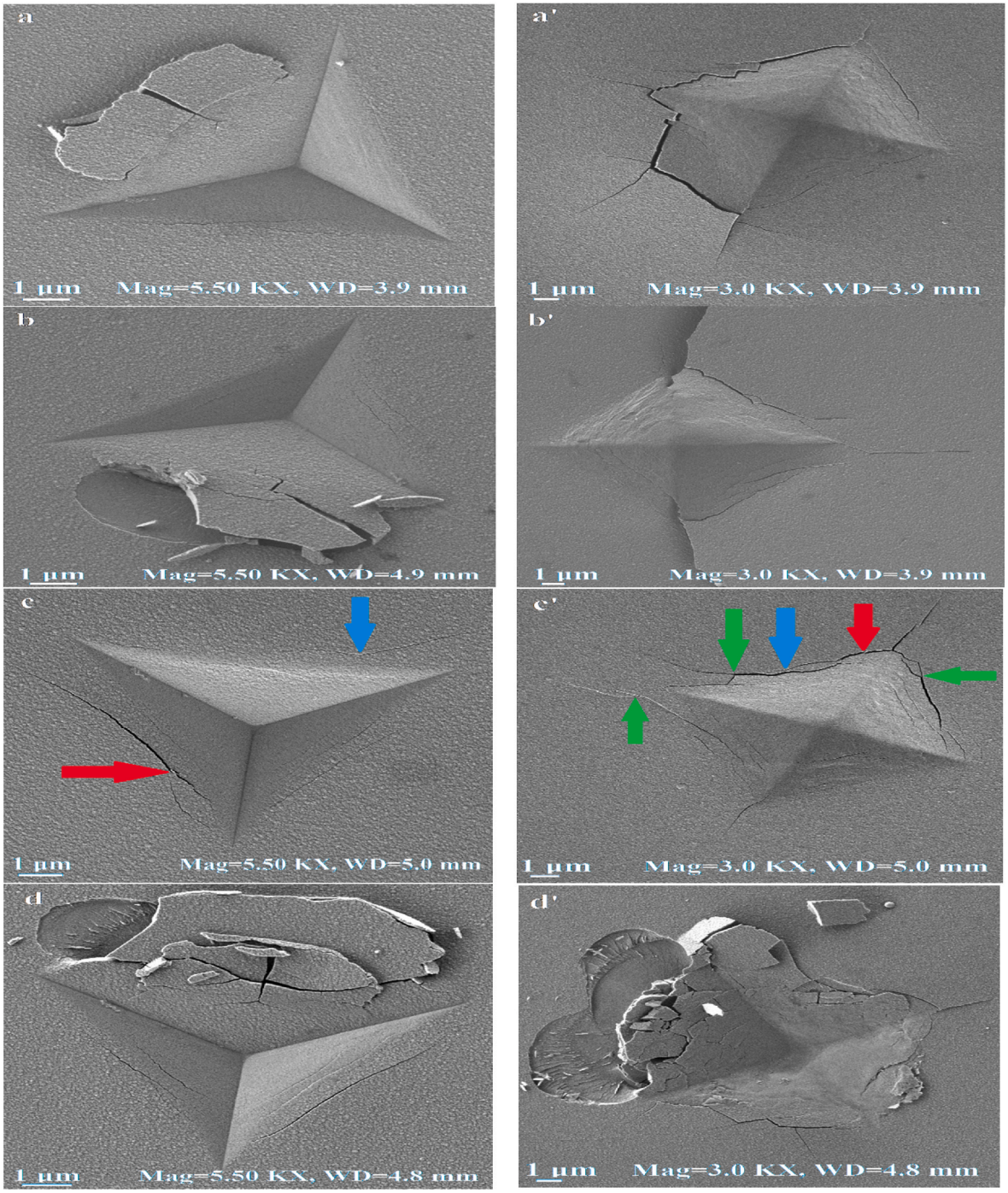

Fig. 7. SEM images of toughness investigation based on high-force indentations; (a = 450 mN, á = 1 N) S0, (b = 450 mN, b´ = 1 N) S40, (c = 450 mN, c´ = 1 N) S60 with crack deflecting-blue arrows-, crack bridging-red arrows- and crack branching-green arrows-, (d = 450 mN, d´ = 1 N) S80 with delamination. (For interpretation of the references to color in this figure legend, the reader is referred to the Web version of this article.).

Higher friction coefficients (more than 0.8) and high friction variation amplitude (more than 0.2 from the average) in these samples are an indicator that it is possible to more detached material. To complement, the pin surfaces after the tests were investigated (see Fig. 12) and it is obvious that the minimum wear occurred to the pin tested against the sample S60. Furthermore, pin surfaces are much more worn-out when tested against S0, S40 and S80 thin films.

To study the wear rate of the coatings, the authors calculate the worn area (A) of the wear tracks (according to Fig. 11a–d and Figs. M6 and M7 in the supplementary file) and present the data in Fig. 11e. Number of cycles is given by C. Because of extremely diverse data of worn area which are extracted from 500, 2000 and 4000 wear cycles, a logarithmic scale was applied. According to the related work [66], it is important to classify coatings by their wear modes; mild wear or severe wear. Thin films with mild wear mode are useful for tribological applications. Based on the regression equations, it is obvious that sample S80 shows the highest wear rate (sudden increase) among the samples and the others follow the low slope linear trend. In contrast, sample S60 gets the lowest wear rate. It shows that the steady-state/mild wear (zone II in Fig. 9) is favorable for contact conditions in mechanical industries. Contrastingly, severe wear occurred in the cases of S0, S40 and S80 because of higher contact area between pin and the damaged surface.

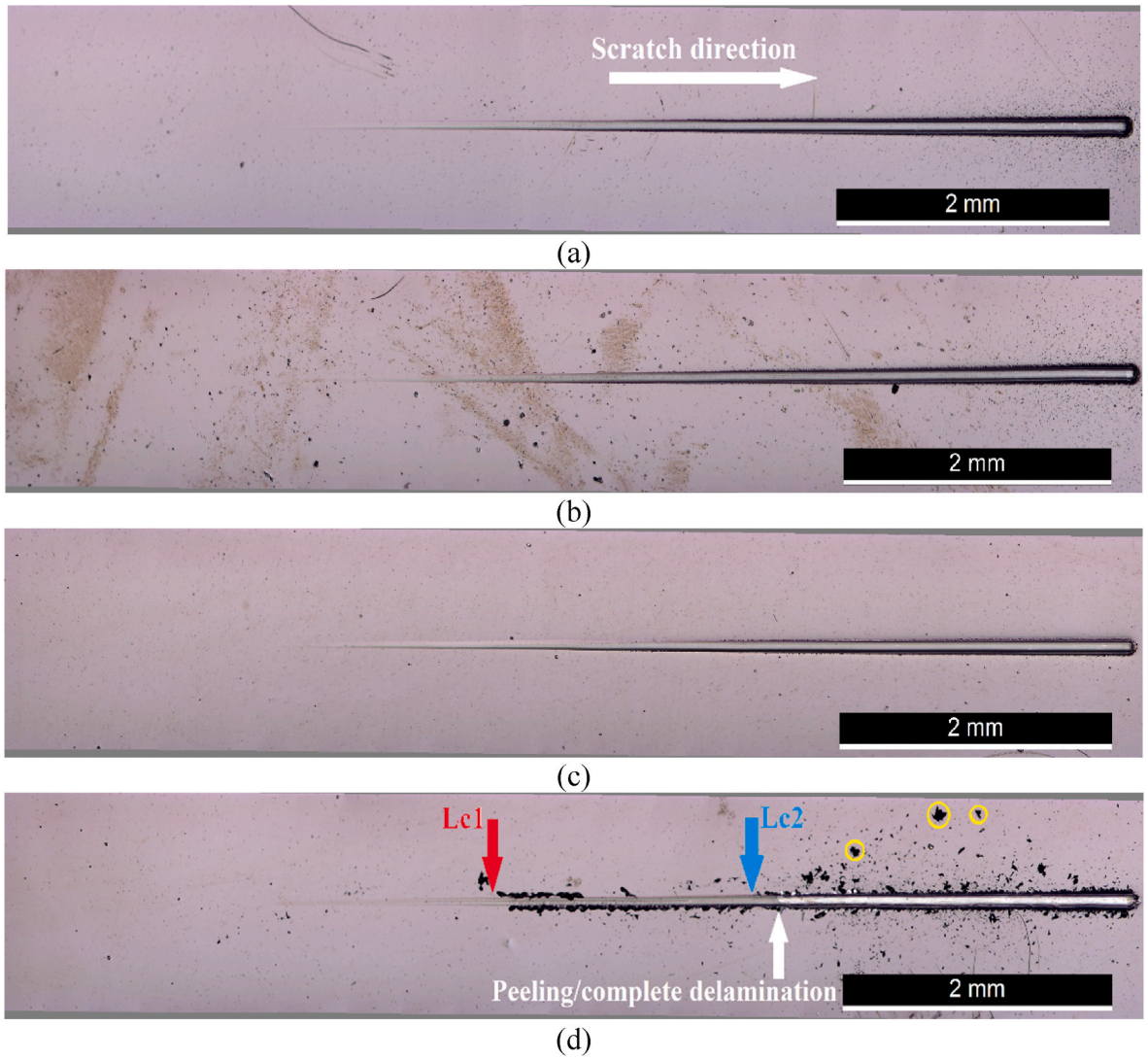

Fig. 8. Scratch images of thin films; (a) S0, (b) S40, (c) S60 and (d) S80 with large flakes presented by yellow circles. (For interpretation of the references to color in this figure legend, the reader is referred to the Web version of this article.).

Table 4
Critical load of thin films.

Sample code	L_C1 [N]	L_C2 [N]	CPR [N^2]
S0	25.5 ±3.6	49.7 ±4.1	617.1
S40	30.8 ±2.9	55.2 ±2.6	751.5
S60	33.9 ±2.7	59.0 ±0.8	851.0
S80	13.9 ±3.1	30.3 ±3.8	227.9

4. Discussion

4.1. Effect of thin film chemistry on mechanical properties

Intrinsic mechanical properties of materials (such as yield stress, Young's modulus and stiffness coefficients) strongly depend on their chemical bonds and phase structure [10,11]. Therefore, in the case of W-Ti-C-N coatings, it is of great importance to analyze the chemistry first and then evaluate the mechanical characteristics. Like similar literature [18,19,22], tungsten carbide/nitride phases as well as titanium carbide/nitride phases, will guarantee high hardness (H > 14.9 GPa, see Fig. 6). Briefly, Fig. 13 shows the effect of coating chemistry/phase structure on mechanical properties of W-Ti-C-N films. When substrate bias voltage values increase, tungsten concentration in thin films will increase up to the maximum value for S60 (19.2%, taken from Table 2) and then decrease. Moreover, in composite coatings, the higher amount of the crystalline phases in an amorphous matrix can be a guarantee to gain higher hardness ($H_{composite} = H_{amorphous\ phase} \times V_{amorphous\ phase} + H_{crystalline\ phase} \times V_{crystalline\ phase}$ provided that $H_{amorphous\ phase} < H_{crystalline\ phases}$ [12]). Based on XRD patterns, amorphous phase is the major phase in the coatings and the crystalline phase amounts play a key role in determining mechanical properties of composite material. According to the Raman analysis of the spectra presented in Fig. 2, the ratio of W_2N intensity to amorphous carbon intensity (which is shown by $I_{max}/I_{a:C}$; as an indicator for the crystalline amount of the coating) has nearly the same trend with increasing substrate bias voltage. These trends are displayed in Fig. 13a. In addition, because of solid solution hardening [67], higher nitrogen content in thin film can cause higher strength by means of lattice micro-strains. Because of these facts, it is predictable that the coating with highest amounts of W, $I_{max}/I_{a:C}$ and N has the highest stiffness and mechanical parameters (sample S60). This trend is illustrated by Fig. 13b which presented the yield strength (YS; which is obtained by the equation of YS ≅ H/3 [6]) and elastic recovery (which is obtained by load-displacement data, Fig. M3 in the supplementary file) of the samples. Some notes must be considered in the case of the low mechanical responses of sample S80 with highest N content and high $I_{max}/I_{a:C}$ ratio. Firstly, the mechanical

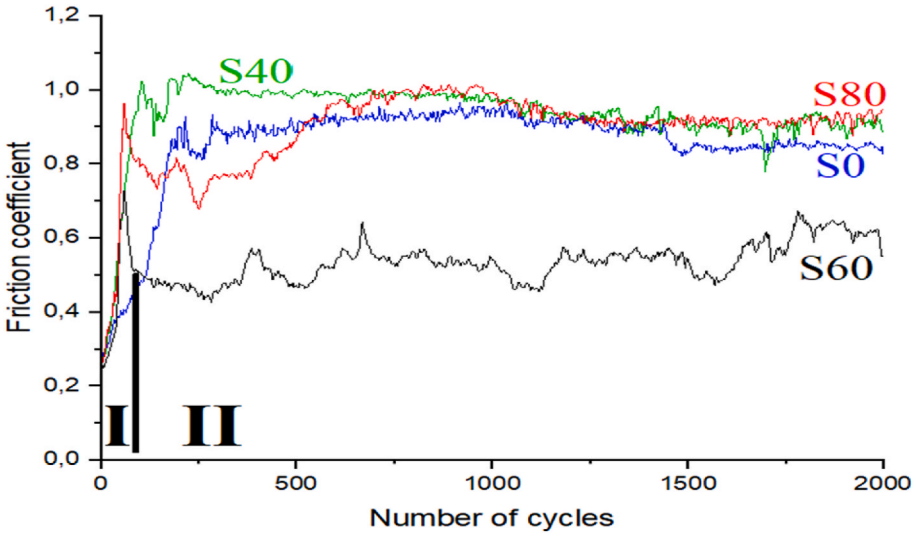

Fig. 9. Friction coefficient of thin films based on pin-on-disk tests.

properties of a film depend strongly on chemical bonds/phases and its morphology and structure. In the case of sample S80, although it has the highest N, however its columnar morphology (shown in Fig. 3d; which is the mark of zone1/T in thin films [7]) generated some micro-voids (between the columns) resulting in low values of the mechanical properties (YS and elastic recovery). This topic will be discussed in more detail in the next section. Secondly, the maximum values of mechanical properties, the conditions with maximum values of W, $I_{max}/I_{a:C}$ and N were obtained simultaneously. In the case of sample S80, W content in sample S80 is the lowest, so the low amount of σ_y and elastic recovery in this film is reasonable. The evolution of H, H/E and H^3/E^2 with this bias voltage shown in Fig. 6 is similar to the trends that are observed in Fig. 13a which also shows the maximum value for S60. The sample S60 has the highest YS (9.7 GPa), elastic recovery (53.5%), H/E (0.116) and H^3/E^2 (0.40). Therefore, it is expected that the resistance to crack initiation and propagation of S60 either under static load (indentation tests) or under dynamic load (sliding tests) has the best behavior. Fracture observations (Figs. 7 and 8), confirm this prediction since no spalling or continuous cracks were generated in sample S60. Unlike S60, the other ones show a different mechanical behavior. With 450 mN static loading, circumferential cracks at one side of the contact area join each other and then result in buckling and partial delamination and chipping/spalling (see Fig. 7a, b and 7d). During 1 N loading of samples S0 and S40, cracks nucleation and growth increased so radial cracks connect to circumferential cracks and failure occurs. This behavior increased in the case of sample S80, probably due to the coating morphology (columnar structure, see Fig. 3d) with minor voids existing in subsurface that facilitate crack propagation, so the catastrophic delamination all over the indented area has occurred. These samples are not resilient enough to carry high loads and fracture takes place extensively. These observations match well with other related works [26,29], that studied the fracture phenomenon of coatings. When two surfaces are in contact, the chemistry is important to avoid sticking/welding two contacting bodies [66]. Besides, it is important to resist high complex stresses applied during sliding. Since the coatings could have a behavior similar to ceramic composite materials, the first mechanism can be neglected. Therefore, the second mode is crucial to study. The plasticity indexes ($\Psi = \acute{E}/H\ (Rq/\acute{R})^{0.5}$ [64]; whereas É is Young's modulus of indenter and the coating and Ŕ is the radius of indenter) of coatings-pin set-up are lower than 0.6, so the contact mode is elastic. Moreover, there is no sign of pile-up in the vicinity of indentations for all of the thin films, so this is another evidence that there is no plastic deformation [23]. Hence, in the case of samples S0, S40 and S80, because of its brittleness ($H/E < 0.1$, $H^3/E^2 < 0.3$ and elastic recovery <50%) and high coefficient of friction (friction coefficient >0.8) cracks expand quickly and spalling will happen in the vicinity of wear scar. With higher loads and distances, as in the scratch tests or with periodic testing in pin-on-disk, delamination and failure will occur. Figs. 8 and 11 can support this behavior with chipping and peeling on the wear track.

4.2. *Effect of thin film topography on mechanical properties*

Extrinsic coatings characteristics like adhesion or tribological performance (like Lc, friction coefficient and wear rate) are strongly dependent on the test conditions (e.g., temperature, humidity/lubrication, counterpart type, diameter, velocity, normal force and contact area) [18,26]. Since the test conditions were kept constant during sliding, the main point is to study the influence of contact geometry between the surfaces involved. As a consequence, studying surface topographical parameters of W-Ti-C-N thin films is necessary to analyze mechanical properties. As it can be seen in section 3.1.2., the morphological and topological characteristics of thin films were described there. It is worth noting that no major defects like macro-particles, buckling or macro-voids at the coating-substrate interface [32] can be detected in the films. This leads to have fine interfacial adhesion. Just because of the bigger columnar morphology of sample S80, some minor voids can exist between lamellar structures. Nevertheless, there is no surprise to see that general topographical factors (Ra, Rq and D) of coatings have nearly the same results because most of the deposition parameters were kept constant (only substrate bias voltage was changed). Interestingly by looking at Table 3, there are major differences in the other fractal features (API, d, GD, Sk and Ku). Fig. 14a illustrates the effect of bias voltage on d and API. Because of homogenous morphology, it can be predictable that sample S60 gets the optimum values of grain size and peak interval. According to Hall-Petch theory [31], hardness and toughness will be increased simultaneously with decreasing grain size. Fig. 14b shows that yield stress follows this rule. Grain size (d) of S60 is minimum while this value is maximum in S80. Moreover, it should be noted that although the average grain size of the films is below 46 nm (see Table 3), the larger grains (see Fig. 4) exist in S0, S40 and S80. Probably this addresses why sample S60 gains the best and sample S80 shows the worst mechanical behavior. In the case of samples S0 and S40, although the average grain size is almost identical, the point is the difference in grain shape. S0 grains have no specific shape so they can degrade surface symmetry. In the case of sample S40 grains represent the spherical shape while oblique extended grains can be seen in Fig. 4d for sample S80. This is because of the oblique growth of columnar

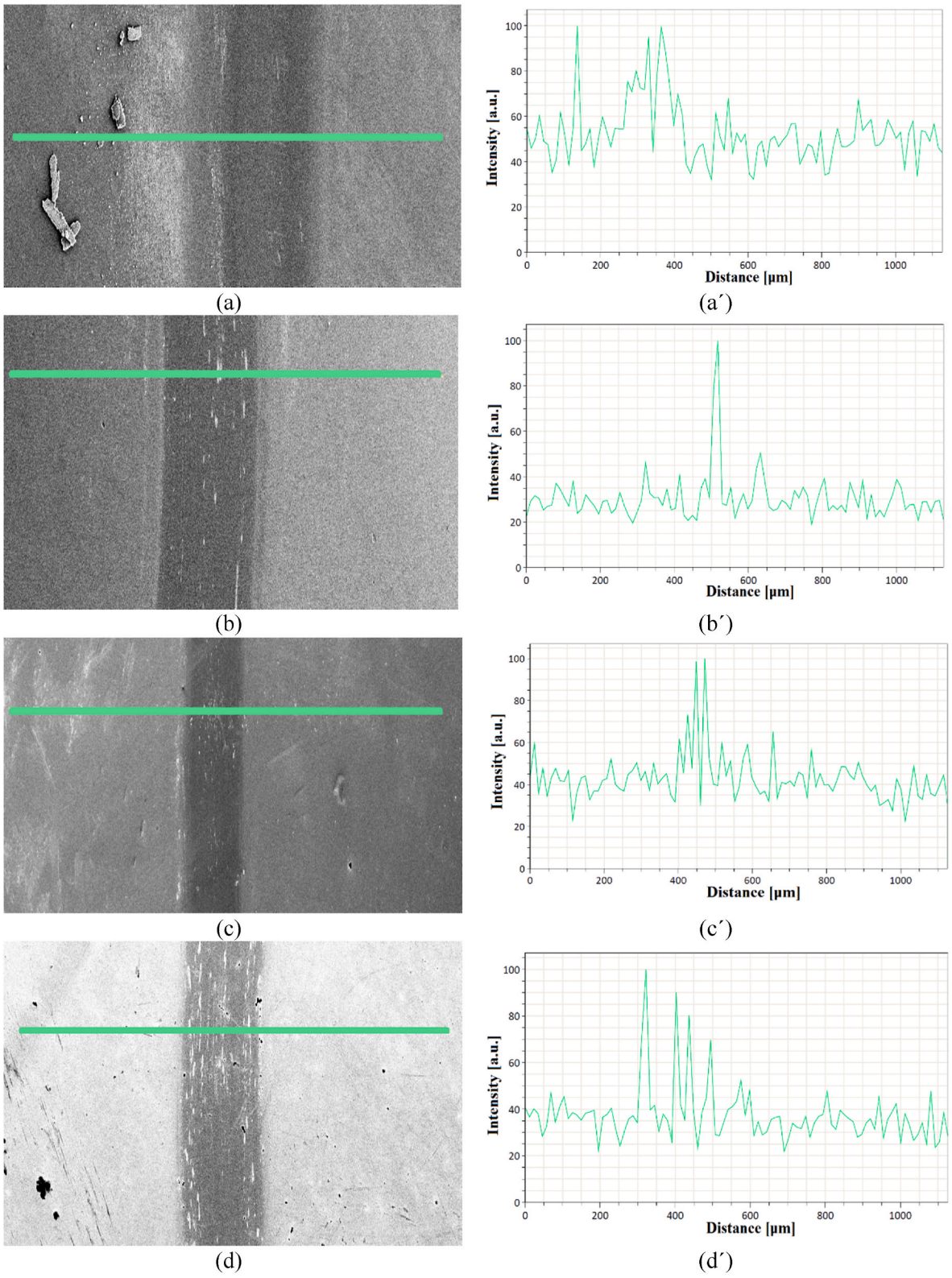

Fig. 10. Top-view wear track and oxygen EDS line of thin films after 2000 cycles pin-on-disk tests; (a, á) S0, (b, b′) S40, (c, c′) S60, (d, d′) S80.

morphology in sample S80 (like the schematic presented in Ref. [7]). Fig. 14c exhibits the effect of grain size on crack resistance and worn area of the coatings. Like yield stress, CPR increases when smaller grains are available. In case of worn area content, although minimum wear rate is achieved by minimum grain size (S60) but the overall trend is not the expected one (highest wear rate for maximum grain size). Further, the regression line cannot be plotted with a high correlation coefficient. This may be due to the wear mechanisms. For example, if oxide tribo-layers (that can improve sliding situation) create [36], the wear loss of S80 can be lower than S0 and S40. To study the top surface quality/uniformity of coating grain density, average peak interval and roughness must be regarded. At first, the effect of peak distance level on crack resistance

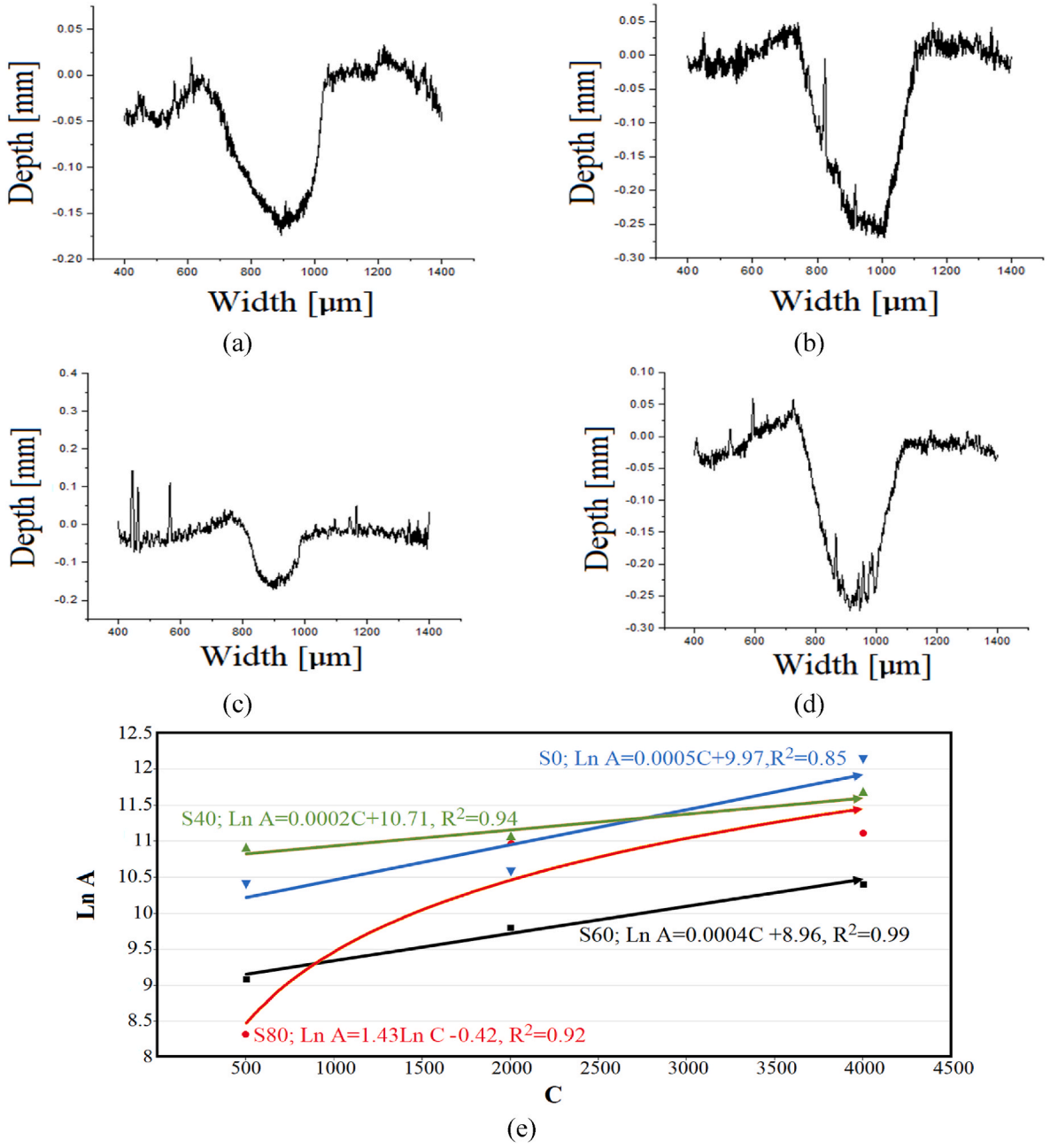

Fig. 11. 2D wear profiles of thin films after 2000 cycles pin-on-disk tests for (a) S0, (b) S40, (c) S60, (d) S80 and wear rate trend for each sample(e).

and wear rate of the coatings is presented in Fig. 14d. It would be predictable that because of the highest compactness of sample S60 (GD is maximum; see Table 3), the maximum peak interval belongs to S60. At the second step, Ra and Rq data of sample S60 are minimums. At last, except S80, others show low positive skewness and Ku is maximum for S60 while the others represent lower amounts. Therefore, it can be concluded that S60 has the lowest peak density and the highest surface symmetry, that makes the coating homogenous and causing less contact with the pin during sliding tests. The important note is that because fractal parameters just investigate the geometry of top atomic layers (near the surface of the coatings) of the coatings, they are unable to explain long-term cyclic tests which are related to deeper materials. Thus, like the grain size effect, the regression line is not given in Fig. 14d. In the case of non-uniform surfaces (S0, S40 and S80) friction fluctuates and coefficient of friction is not stable. This description can be seen in Fig. 9, whereas the running-in period (stage I in Fig. 9) continued for more than 500 cycles for S0, S40 and S80 and lasted nearly 120 cycles in the case of S60. This means that steady state wear (stage II in Fig. 9) occurs in sample S60 while for others high unstable wear develops. Moreover, the high levels of friction coefficient can lead to severe wear which can be seen in Fig. 11. As S60 shows the minimum contact area (minimum pin worn area which shows in Fig. 12) and maximum adhesion strength (maximum CPR value), minimum wear rate is rational and can be a superior candidate to apply in machining industries (e. g. die machining).

At the end, it is important to analyze the differences between the optimum sample (S60) and the worst one (S80). Nano-composite coating with the highest content of W and uniform featureless morphology (S60) can deflect, bridge and branch cracks during loading. Previous papers [24,25] proved that these toughening mechanisms for ceramics can enhance work durability, so S60 can bear scratch and wear conditions without delamination. In contrast, nano-composite coating

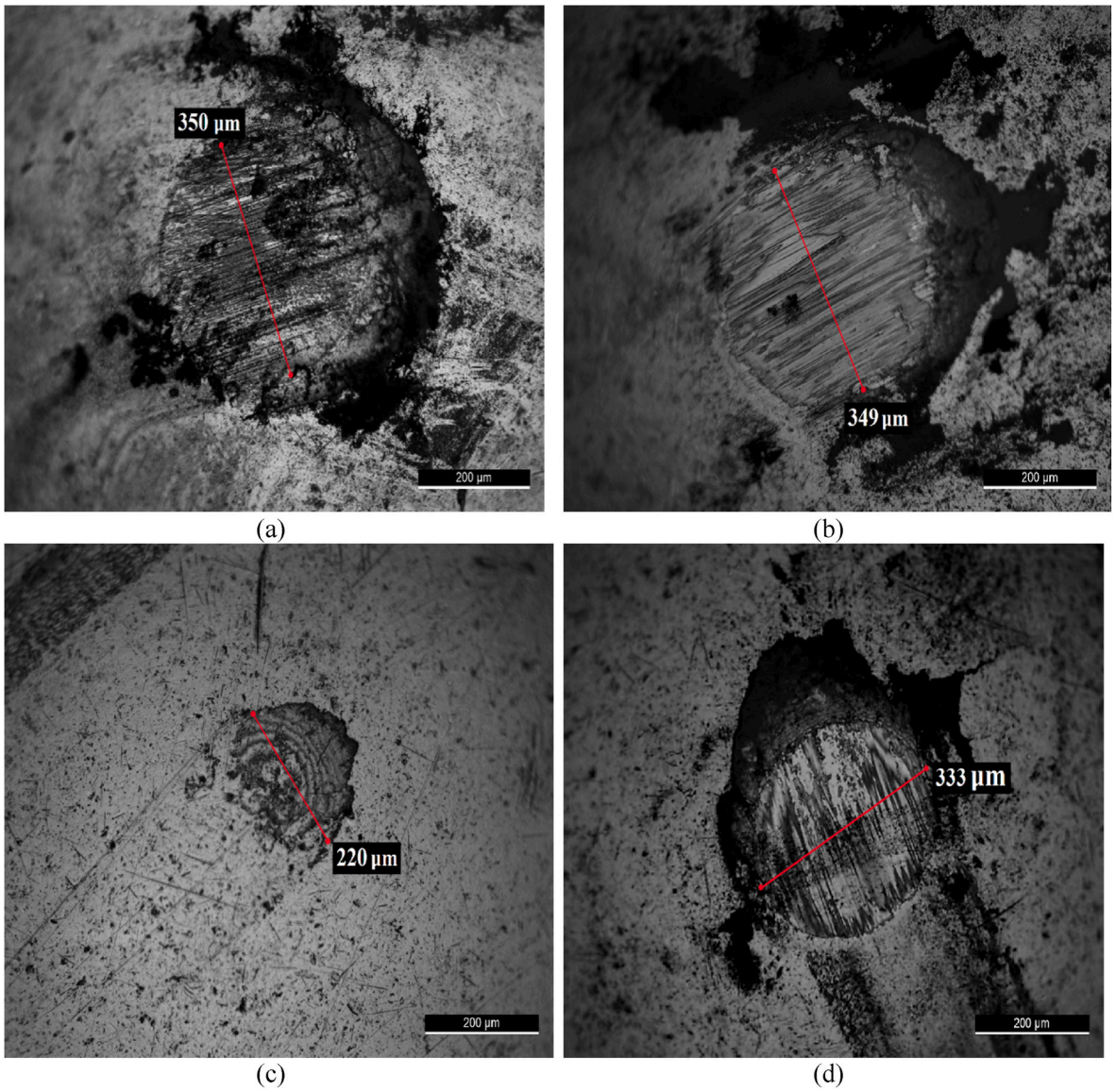

Fig. 12. Surface images of pins after 2000 cycles wear tests with contact diameter; (a) slid along S0, (b) slid along S40, (c) slid along S60 and (d) slid along S80.

with lowest content of W and textured asymmetric morphology (S80) may facilitate crack initiation and propagation. Thus, it is noteworthy to study the quick delamination procedure of sample S80 to see the effect of thin film structure on failure behavior and to avoid unfavorable design during manufacturing process. Based on the representative volume element (RVE) method [60], Fig. 15 shows a model of catastrophic fracture graphically. Applying HIPIMS-DCMS with fine surface cleaning before the deposition, makes it real and significant to assume that the morphology of sample S80 in various sites follows the characteristics of the cross-sectional SEM image presented in Figs. 3d and 4d. Hence, the assumption that physical properties of one element (SEM image) represent properties of the total system is sensible. Therefore, using Figs. 3d and 4d, a representative volume element is introduced for further modeling (Fig. 15a). Because of columnar growth (Fig. 3d) and textured grains (Fig. 4d and Fig. M1d in the supplementary file), it is logical that some sharp valleys (blue circles in Fig. M2d in the supplementary material) in the stress field can act like a crack facilitator (blue boundaries in Fig. 15b). This idea (subsurface voids in elastoplastic contact are best locations for crack growth) is in good agreement with delamination wear theory suggested by Fleming and Suh [35]. As it can be seen in Fig. 15c, during loading some cracks will nucleate and develop in special paths. Based on the work done by Meindlhumer et al. [40], the paths are columnar boundaries because these boundaries have low cohesive energy. Increasing load (or cyclic motion) can cause quick/sudden crack propagation and join each other until approaching the coating-substrate interface (red boundaries in Fig. 15d). This river-like propagation pattern may be related to two distinct mechanisms which occurred at the same time. First and foremost, the path is quite suitable for crack expansion because linear micro-voids existed in the lamellar/columnar morphology of S80. Last but not least, because of lower toughness values ($H/E < 0.09$ and $H^3/E^2 < 0.12$), toughening mechanisms cannot be activated and not only the crack tips will not be arrested (the concept of crack tip opening displacement was presented elsewhere [34]) but also, they propagate rapidly. Moreover, cracks simply extend and materials detach from the coatings. Hence, large flakes (brown pieces in Fig. 15e) and peeling will be generated as soon as possible and complete delamination and brittle fracture occur.

5. Conclusions

Structural characterization of W-Ti-C-N thin films was done by several complementary methods. Moreover, the mechanical properties

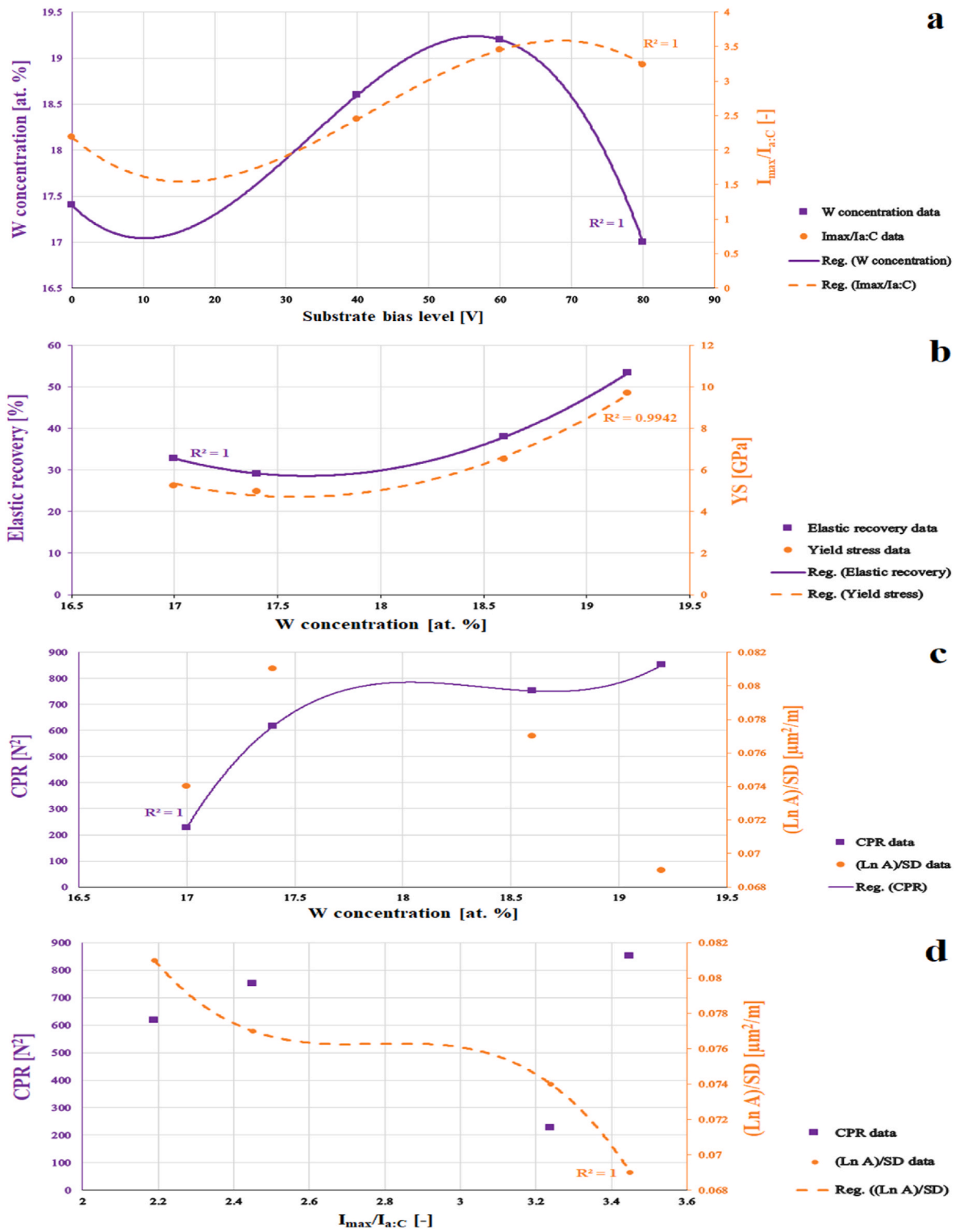

Fig. 13. (a) effect of substrate bias voltage on tungsten percentage and crystallinity of thin films, (b) effect of tungsten percentage on elastic recovery and yield strength of thin films, (c) effect of tungsten percentage on crack resistance and wear rate of thin films, (d) effect of crystallinity on crack resistance and wear rate of thin films.

of the coatings are comprehensively studied. Hence, it can be concluded that:

1 Increasing substrate bias voltage affects the chemical composition of thin films. Up to −60 V tungsten content of the coatings increased, then a significant decrease was observed. Moreover, all the coatings show nano-composite phase structure.
2 Based on the fractal analysis data, in order to gain uniform and symmetrical surfaces, grain density (302.2 µm-2) and kurtosis should be maximum (2.83) while grain size (42.8 nm) and roughness (1.18

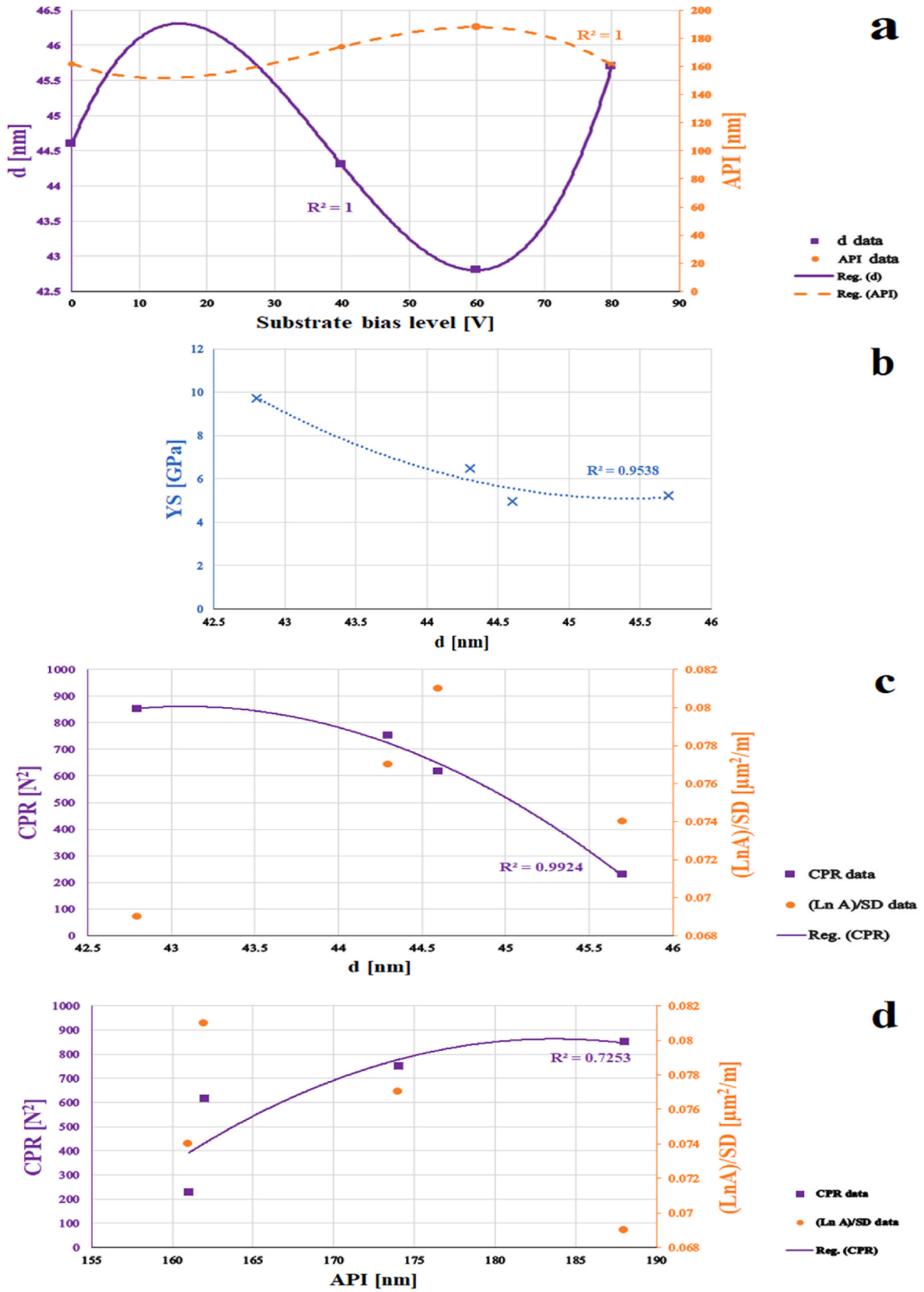

Fig. 14. (a) effect of substrate bias voltage on grain size and average peak interval of coatings, (b) effect of grain size on yield stress, (c) effect of grain size on crack propagation resistance and wear rate, (d) effect of average peak interval on crack propagation resistance and wear rate.

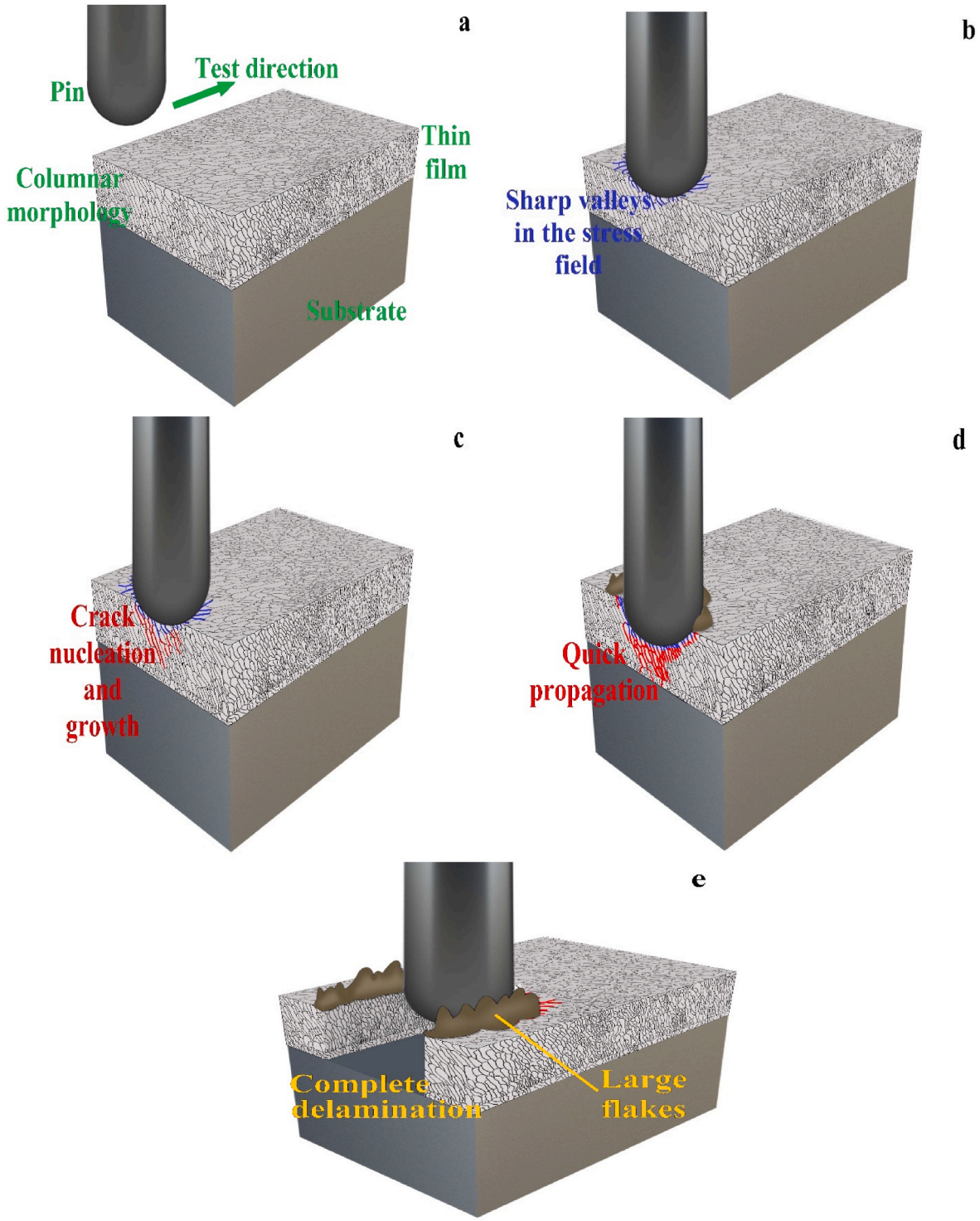

Fig. 15. Schematic of crack growth model for sudden and catastrophic delamination occurred in sample S80 based on cross-sectional SEM image morphology; (a) before loading, (b) initial stage of loading-sensitive sites for crack nucleation, (c) crack nucleation and growth, (d) cracks joining and approaching the substrate-coating interface, (e) complete delamination and fracture .

nm) should get the minimum levels. Furthermore, it is of great importance to avoid negative skewness and textured grains.

3 SEM observations before and after mechanical testing show that the coating with higher compactness and H/E ratios can withstand high loads/cycles without sudden delamination and fracture. As a result, crack propagation resistance quantity of this sample (S60) is maximum and the wear rate is minimum.

4 Worst wear characteristics reported for the case of sample S80. The river model was introduced to indicate the material cut-off. Because of voids located in columnar morphology, crack growth remarkably extended like a river pattern and after higher loads/cycles this network of minor cracks meet each other and make the material detached from the surface.

CRediT authorship contributions statement

S. A. Ataie: Methodology, Software, Data Curation, Writing - Original Draft. **M. Soltanieh:** Writing - Review & Editing, Supervision. **R. Naghizadeh:** Methodology, Data Curation. **A. Cavaleiro:** Writing - Review & Editing, Supervision. **M. Evaristo:** Investigation, Formal analysis. **F. Fernandes:** Formal analysis, Visualization. **F. Ferreira:** Resources, Conceptualization, Validation.

Declaration of competing interest

The authors declare that they have no known competing financial interests or personal relationships that could have appeared to influence the work reported in this paper.

Data availability

Data will be made available on request.

Acknowledgement

This research is sponsored by national funds through FCT – Fundação para a Ciência e a Tecnologia, under the project UIDB/00285/2020.

Appendix A. Supplementary data

Supplementary data to this article can be found online at https://doi.org/10.1016/j.wear.2023.204654.

References

[1] S. Ramalingam, W.O. Winer, REACTIVELY SPUTTERED TiN COATINGS FOR TRIBOLOGICAL APPLICATIONS, Thin Solid Films 73 (1980) 267–274, https://doi.org/10.1016/0040-6090(80)90489-7.
[2] M. Lepicka, M. Gradzka-Dahlke, D. Pieniak, K. Pasierbiewicz, K. Krynska, A. Niewczas, Tribological performance of titanium nitride coatings: a comparative study on TiN coated stainless steel and titanium alloy, Wear 422 (2019) 68–80, https://doi.org/10.1016/j.wear.2019.01.029.
[3] A.K. Mishra, H. Gopalan, M. Hans, C. Kirchlechner, J.M. Schneider, G. Dehm, B. N. Jaya, Strategies for damage tolerance enhancement in metal/ceramic thin films: lessons learned from Ti/TiN, Acta Mater. 228 (2022), 117777, https://doi.org/10.1016/j.actamat.2022.117777.
[4] Y. Wang, N. He, C. Wang, J. Li, W. Guo, Y. Sui, J. Lan, Microstructure and tribological performance of (AlCrWTiMo)N film controlled by substrate temperature, Appl. Surf. Sci. 574 (2022), 151677, https://doi.org/10.1016/j.apsusc.2021.151677.
[5] M. Herbster, J. Döring, J. Nohava, C.H. Lohmann, T. Halle, J. Bertrand, Retrieval study of commercially available knee implant coatings TiN, TiNbN and ZrN on TiAl6V4 and CoCr28Mo6, J. Mech. Behav. Biomed. Mater. 112 (2020), https://doi.org/10.1016/j.jmbbm.2020.104034.
[6] K.E. Davies, B.K. Gan, D.R. McKenzie, M.M.M. Bilek, M.B. Taylor, D.G. McCulloch, B.A. Latella, Correlation between stress and hardness in pulsed cathodic arc deposited titanium/vanadium nitride alloys, J. Phys. Condens. Matter 16 (2004) 7947–7954, https://doi.org/10.1088/0953-8984/16/45/017.
[7] J. Musil, J. Vlček, Magnetron sputtering of hard nanocomposite coatings and their properties, Surf. Coating. Technol. 142–144 (2001) 557–566, https://doi.org/10.1016/S0257-8972(01)01139-2.
[8] T.W. Hsu, G. Greczynski, R. Boyd, S. Kolozsvári, P. Polcik, S. Bolz, B. Bakhit, M. Odén, Influence of Si content on phase stability and mechanical properties of TiAlSiN films grown by AlSi-HiPIMS/Ti-DCMS co-sputtering, Surf. Coating. Technol. 427 (2021), https://doi.org/10.1016/j.surfcoat.2021.127661.
[9] V.F.C. Sousa, F.J.G. Silva, H. Lopes, R.C.B. Casais, A. Baptista, G. Pinto, R. Alexandre, Wear behavior and machining performance of TiAlSiN-coated tools obtained by dc ms and hipims: a comparative study, Materials 14 (2021) 1–18, https://doi.org/10.3390/ma14185122.
[10] C.P. Constable, J. Yarwood, W.D. Münz, Raman microscopic studies of PVD hard coatings, Surf. Coating. Technol. 116–119 (1999) 155–159, https://doi.org/10.1016/S0257-8972(99)00072-9.
[11] S. Veprek, M.G.J. Veprek-Heijman, P. Karvankova, J. Prochazka, Different approaches to superhard coatings and nanocomposites, Thin Solid Films 476 (2005) 1–29, https://doi.org/10.1016/J.TSF.2004.10.053.
[12] R.W. Armstrong, The hardness and strength properties of WC-Co composites, Materials 4 (2011) 1287–1308, https://doi.org/10.3390/ma4071287.
[13] A. Pawbake, R. Waykar, A. Jadhavar, R. Kulkarni, V. Waman, A. Date, D. Late, H. Pathan, S. Jadkar, Wide band gap and conducting tungsten carbide (WC) thin films prepared by hot wire chemical vapor deposition (HW-CVD) method, Mater. Lett. 183 (2016) 315–317, https://doi.org/10.1016/j.matlet.2016.07.132.
[14] L. Haus, M. Wildfeuer, J.E. Grochowski, J. Wockel, M. Muller, F. Kohn, W. Schulz, C. Wustefeld, D. Rafaja, J. Albrecht, Wear properties of carbon-rich tungsten carbide films, Wear 488 (2022), 204146, https://doi.org/10.1016/j.wear.2021.204146.
[15] M.L. Addonizio, A. Castaldo, A. Antonaia, E. Gambale, L. Iemmo, Influence of process parameters on properties of reactively sputtered tungsten nitride thin films, J. Vac. Sci. Technol. A Vacuum, Surfaces, Film. 30 (2012), 031506, https://doi.org/10.1116/1.3698399.
[16] Z. Li, H. Zhang, W. He, L. Xu, G. Zhang, X. Nie, B. Liao, Y. Li, Tribological performance of GLC, WC/GLC and TiN films on the carburized M50NiL steel, Surf. Coating. Technol. 361 (2019) 1–8, https://doi.org/10.1016/j.surfcoat.2019.01.038.
[17] W. Pawlak, K.J. Kubiak, B.G. Wendler, T.G. Mathia, Wear resistant multilayer nanocomposite WC1-x/C coating on Ti-6Al-4V titanium alloy, Tribol. Int. 82 (2015) 400–406, https://doi.org/10.1016/j.triboint.2014.05.030.
[18] S.A. Ataie, M. Soltanieh, R. Naghizadeh, M. Ahmadi, M. Ghanaatshoar, Effects of substrate temperature and reactive gas flow rate on the crystalline ceramic phases formation and tribological properties of W–Ti–Co–C–N thin films produced by co-sputtering, Ceram. Int. 46 (2020) 29137–29149, https://doi.org/10.1016/j.ceramint.2020.08.087.
[19] M.T. Vieira, A. Cavaleiro, B. Trindade, The effects of a third element on structure and properties of W-C/N, Surf. Coating. Technol. 151–152 (2002) 495–504, https://doi.org/10.1016/S0257-8972(01)01640-1.
[20] A. Nossa, A. Cavaleiro, Mechanical behaviour of W-S-N and W-S-C sputtered coatings deposited with a Ti interlayer, Surf. Coating. Technol. 163–164 (2003) 552–560, https://doi.org/10.1016/S0257-8972(02)00622-9.
[21] A. Cavaleiro, B. Trindade, M.T. Vieira, Influence of Ti addition on the properties of W–Ti–C/N sputtered films, Surf. Coating. Technol. 174 –175 (2003) 68–75, https://doi.org/10.1016/S0257-8972(03)00328-1.
[22] J.S. Yoon, H.S. Myung, J.G. Han, J. Musil, A study on the synthesis and microstructure of WC-TiN superlattice coating, Surf. Coating. Technol. 131 (2000) 372–377, https://doi.org/10.1016/S0257-8972(00)00808-2.
[23] W.B. Liao, H. Zhang, Z.Y. Liu, P.F. Li, J.J. Huang, C.Y. Yu, Y. Lu, High strength and deformation mechanisms of Al0.3CoCrFeNi high-entropy alloy thin films fabricated by magnetron sputtering, Entropy 21 (2019) 1–9, https://doi.org/10.3390/e21020146.
[24] R.W. Steinbrech, Toughening mechanisms for ceramic materials, J. Eur. Ceram. Soc. 10 (1992) 131–142, https://doi.org/10.1016/0955-2219(92)90026-A.
[25] F.F. Ge, H.S. Sen, N. Daghbouj, M. Callisti, Y.J. Feng, B.S. Li, P. Zhu, P. Li, F. P. Meng, T. Polcar, F. Huang, Toughening mechanisms in V-Si-N coatings, Mater. Des. 209 (2021), https://doi.org/10.1016/j.matdes.2021.109961.
[26] S. Zhang, X. Zhang, Toughness evaluation of hard coatings and thin films, Thin Solid Films 520 (2012) 2375–2389, https://doi.org/10.1016/j.tsf.2011.09.036.
[27] R. Alias, R. Mahmoodian, M. Rizwan, M.H. Abd Shukor, Study the effect of thermal annealing on adhesion strength of Silver-Tantalum Oxide thin film deposited by reactive magnetron sputtering, J. Adhes. Sci. Technol. 33 (2019) 1626–1643, https://doi.org/10.1080/01694243.2018.1549770.
[28] S. Zhang, D. Sun, Y. Fu, H. Du, Toughness measurement of thin films: a critical review, Surf. Coating. Technol. 198 (2005) 74–84, https://doi.org/10.1016/j.surfcoat.2004.10.021.
[29] Z. Tan, X. Wu, G. Yang, J. Guo, W. Zhu, Structure, mechanical, and micro-scratch behavior of Ta-Hf-C solid solution coating deposited by non-reactive magnetron sputtering, Materials 15 (2022) 4489, https://doi.org/10.3390/ma15134489.
[30] X. Li, D. Diao, B. Bhushan, Fracture mechanisms of thin amorphous carbon films in nanoindentation, Acta Mater. 45 (1997) 4453–4461, https://doi.org/10.1016/S1359-6454(97)00143-2.
[31] R.W. Armstrong, Hall-Petch analysis of dislocation pileups in thin material layers and in nanopolycrystals, J. Mat. Res. Soc. 28 (2013) 1792–1798, https://doi.org/10.1557/jmr.2013.10.
[32] P. Panjan, M. Čekada, M. Panjan, D. Kek-Merl, Growth defects in PVD hard coatings, Vacuum 84 (2009) 209–214, https://doi.org/10.1016/j.vacuum.2009.05.018.
[33] K. Hebbar Kannur, T. Bin Yaqub, T. Huminiuc, T. Polcar, C. Pupier, C. Héau, A. Cavaleiro, Synthesis and structural properties of Mo-S-N sputtered coatings, Appl. Surf. Sci. 527 (2020), 146790, https://doi.org/10.1016/j.apsusc.2020.146790.
[34] Y. Gu, K. Chen, R. Liu, M.X. Yao, R. Collier, Indentation modeling study of temperature-dependent fracture toughness of brittle coating on ductile substrate based on microcrack formation theory, Surf. Coating. Technol. 309 (2017) 536–544, https://doi.org/10.1016/j.surfcoat.2016.12.016.
[35] J.R. Fleming, N.P. Suh, Mechanics of crack propagation in delamination wear, Wear 44 (1977) 39–56, https://doi.org/10.1016/0043-1648(77)90083-7.
[36] D. Wainstein, A. Kovalev, Tribooxidation as a way to improve the wear resistance of cutting tools, Coatings 8 (2018) 1–9, https://doi.org/10.3390/coatings8060223.
[37] N. Boughrara, Z. Benzarti, A. Khalfallah, M. Evaristo, A. Cavaleiro, Comparative study on the nanomechanical behavior and physical properties influenced by the epitaxial growth mechanisms of GaN thin films, Appl. Surf. Sci. 579 (2022), 152188, https://doi.org/10.1016/j.apsusc.2021.152188.
[38] M. Gassner, M. Rebelo de Figueiredo, N. Schalk, R. Franz, C. Weiß, H. Rudigier, H. Holzschuh, W. Bürgin, M. Pohler, C. Czettl, C. Mitterer, Energy consumption and material fluxes in hard coating deposition processes, Surf. Coating. Technol. 299 (2016) 49–55, https://doi.org/10.1016/j.surfcoat.2016.04.062.
[39] V. Collado Cipres, E.L. Dalibon, J. García, L. Escalada, J.J. Roa, E. Jimenez-Pique, F. Soldera, S.P. Bruhl, S. Simison, L. Llanes, A.D. Sosa, Contact fatigue behavior of CVD coated cemented carbides in dry and wet conditions, Wear 492 (2022), 204215, https://doi.org/10.1016/j.wear.2021.204215.

[40] M. Meindlhumer, T. Ziegelwanger, J. Zalesak, M. Hans, L. Löfler, S. Spor, N. Jäger, A. Stark, H. Hruby, R. Daniel, D. Holec, J.M. Schneider, C. Mitterer, J. Keckes, Precipitation-based grain boundary design alters inter- to trans-granular fracture in AlCrN thin films, Acta Mater. 237 (2022), 118156, https://doi.org/10.1016/j.actamat.2022.118156.
[41] B. Karunagaran, R.T. Rajendra Kumar, V. Senthil Kumar, D. Mangalaraj, S. K. Narayandass, G. Mohan Rao, Structural characterization of DC magnetron-sputtered TiO2 thin films using XRD and Raman scattering studies, Mater. Sci. Semicond. Process. 6 (2003) 547–550, https://doi.org/10.1016/j.mssp.2003.05.012.
[42] J. Bohlmark, M. Lattemann, J.T. Gudmundsson, A.P. Ehiasarian, Y. Aranda Gonzalvo, N. Brenning, U. Helmersson, The ion energy distributions and ion flux composition from a high power impulse magnetron sputtering discharge, Thin Solid Films 515 (2006) 1522–1526, https://doi.org/10.1016/j.tsf.2006.04.051.
[43] J.T. Gudmundsson, The high power impulse magnetron sputtering discharge as an ionized physical vapor deposition tool, Vacuum 84 (2010) 1360–1364, https://doi.org/10.1016/j.vacuum.2009.12.022.
[44] Y. Xu, G. Li, G. Li, F. Gao, Y. Xia, Effect of bias voltage on the growth of super-hard (AlCrTiVZr)N high-entropy alloy nitride films synthesized by high power impulse magnetron sputtering, Appl. Surf. Sci. 564 (2021) 1–10, https://doi.org/10.1016/j.apsusc.2021.150417.
[45] F. Ferreira, R. Serra, J.C. Oliveira, A. Cavaleiro, Effect of peak target power on the properties of Cr thin films sputtered by HiPIMS in deep oscillation magnetron sputtering (DOMS) mode, Surf. Coating. Technol. 258 (2014) 249–256, https://doi.org/10.1016/j.surfcoat.2014.09.020.
[46] F. Ferreira, A. Cavaleiro, J.C. Oliveira, Effect of substrate biasing on the structure and properties of tantalum coatings deposited using HIPIMS in deep oscillation magnetron sputtering mode, Metals 10 (2020) 1618, https://doi.org/10.3390/met10121618.
[47] A. Bahr, T. Glechner, T. Wojcik, A. Kirnbauer, M. Sauer, A. Foelske, O. Hunold, E. Ntemou, E. Pitthan, D. Primetzhofer, H. Riedl, R. Hahn, Non-reactive HiPIMS deposition of NbC x thin films : effect of the target power density on structure-mechanical properties, Surf. Coating. Technol. 444 (2022), https://doi.org/10.1016/j.surfcoat.2022.128674.
[48] F. Ferreira, J.C. Oliveira, A. Cavaleiro, CrN thin films deposited by HiPIMS in DOMS mode, Surf. Coating. Technol. 291 (2016) 365–375, https://doi.org/10.1016/j.surfcoat.2016.02.064.
[49] F. Ferreira, A. Cavaleiro, J. Oliveira, Tribological performance of DLC coatings deposited by DOMS in mixed Ar-Ne discharges, Mater. Lett. 285 (2021), https://doi.org/10.1016/j.matlet.2020.129056.
[50] H.S. Ahn, P.D. Cuong, K.H. Shin, K.S. Lee, Tribological behavior of sputtered boron carbide coatings and the influence of processing gas, Wear 259 (2005) 807–813, https://doi.org/10.1016/j.wear.2005.02.096.
[51] C.D. Boeira, L.M. Leidens, A.F. Michels, R. Serra, M. Evaristo, F. Fernandes, A. Cavaleiro, C.A. Figueroa, Influence of base pressure prior to deposition on the adhesion behaviour of carbon thin films on steel, Appl. Surf. Sci. Adv. 2 (2020), 100034, https://doi.org/10.1016/j.apsadv.2020.100034.
[52] T. Kumada, M. Ohtsuka, H. Fukuyama, Influence of substrate temperature on the crystalline quality of AlN layers deposited by RF reactive magnetron sputtering, AIP Adv. 5 (2015), https://doi.org/10.1063/1.4906796.
[53] M. Mickan, U. Helmersson, D. Horwat, Effect of substrate temperature on the deposition of Al-doped ZnO thin films using high power impulse magnetron sputtering, Surf. Coating. Technol. 347 (2018) 245–251, https://doi.org/10.1016/j.surfcoat.2018.04.089.
[54] Q. Ma, L. Li, Y. Xu, J. Gu, L. Wang, Y. Xu, Effect of bias voltage on TiAlSiN nanocomposite coatings deposited by HiPIMS, Appl. Surf. Sci. 392 (2017) 826–833, https://doi.org/10.1016/j.apsusc.2016.09.028.
[55] J.C. Ding, H. Mei, Q. Li, Z. Zhao, Y. Shen, L. Cheng, R. Wang, W. Gong, Q. Wang, Microstructure, mechanical and tribological properties of Mo–V–Cu–N coatings prepared by HIPIMS technique, Ceram. Int. 48 (2022) 10704–10712, https://doi.org/10.1016/j.ceramint.2021.12.285.
[56] R. Serra, F. Ferreira, A. Cavaleiro, J.C. Oliveira, HiPIMS pulse shape influence on the deposition of diamond-like carbon films, Surf. Coating. Technol. 432 (2022), 128059, https://doi.org/10.1016/j.surfcoat.2021.128059.
[57] G.R. Anstis, P. Chantikul, B.R. Lawn, D.B. Marshall, A critical evaluation of indentation techniques for measuring fracture toughness: I, direct crack measurement, J. Ame. Cer. Sc. (1981) 533–538, https://doi.org/10.1111/j.1151-2916.1981.tb10320.x.
[58] G.M. Pharr, W.C. Oliver, Measurement of thin film mechanical properties using nanoindentation, MRS Bull. 17 (1992) 28–33, https://doi.org/10.1557/S0883769400041634.
[59] G.M. Pharr, Measurement of mechanical properties by ultra-low load indentation, Mater. Sci. Eng. 253 (1998) 151–159, https://doi.org/10.1016/s0921-5093(98)00724-2.
[60] D. Brands, D. Balzani, L. Scheunemann, J. Schröder, H. Richter, D. Raabe, Computational modeling of dual-phase steels based on representative three-dimensional microstructures obtained from EBSD data, Arch. Appl. Mech. 86 (2016) 575–598, https://doi.org/10.1007/s00419-015-1044-1.
[61] R. Singh, M. Gupta, D.M. Phase, S.K. Mukherjee, XANES and XRR study on phase evolution of TiO 2 films developed using HiPIMS, Mater. Sci. Eng., B 283 (2022), 115827, https://doi.org/10.1016/j.mseb.2022.115827.
[62] D.L. Costa E Silva, L.R. Pires Kassab, A.D. dos Santos, M.F. Pillis, Evaluation of carbon thin films using Raman spectroscopy, Mater. Res. 21 (2018) 1–6, https://doi.org/10.1590/1980-5373-MR-2017-0787.
[63] A.K.M.S. Chowdhury, D.C. Cameron, M.S.J. Hashmi, Vibrational properties of carbon nitride films by Raman spectroscopy, Thin Solid Films 332 (1998) 62–68, https://doi.org/10.1016/S0040-6090(98)00984-5.
[64] C.A. Kotwal, B. Bhushan, Contact analysis of non-Gaussian surfaces for minimum static and kinetic friction and wear, Tribol. Trans. 39 (1996) 890–898, https://doi.org/10.1080/10402009608983609.
[65] A.G. Evans, E.A. Charles, Fracture toughness determinations by indentation, J. Ame. Cer. Sc. (1976) 371–372, https://doi.org/10.1111/j.1151-2916.1976.tb10991.x.
[66] L. Ma, K. Eom, J. Geringer, T. Jun, Literature review on fretting wear and contact mechanics of tribological coatings, Coatings 9 (2019) 501, https://doi.org/10.3390/coatings9080501.
[67] J. Pelleg, Mechanical Properties of Materials, Solid Mechanics and its Applications, Springer Dordrecht, 2013, https://doi.org/10.1007/978-94-007-4342-7.